Internal dynamics in condensed matter, as studied by spin relaxation: some examples from 75 years

Erik B. Karlsson[a]

Department of Physics and Astronomy, Uppsala University, P. O. Box 516, SE-75120 Uppsala, Sweden

Abstract The present year 2021 celebrates the 75th anniversary of the nuclear magnetic resonance method (NMR), which has had an immense importance for several branches of physics, chemistry and biology. The splitting of resonances and the shifts in their positions are seemingly inexhaustible sources of information for organic chemistry and biology. It was first introduced for the study of nuclear spins and their associated magnetic properties and when it was observed that resonance lines were broadened by the action of fluctuating local magnetic fields it was first seen as a limitation for the exact determination of nuclear properties. However, it was soon realized that the broadening contained important information on the dynamics of atoms, molecules or cooperative spin systems surrounding the nuclei and spin perturbations became a well-developed tool for investigation of internal dynamics in liquids and solids, over time-ranges from seconds down to femtoseconds. The present article is an attempt to review this latter line of development and to pick out a series of examples of internal dynamics in different physical systems published over the past 75 years. Examples include motions of particles in solids, magnetic resonance imaging (MRI), critical phenomena around phase transitions, functioning of biomolecules and recent applications to spintronics and quantum computing. Other spin-based spectroscopies followed in the tracks of NMR with use of electron spins (in electron spin resonance ESR also called electron paramagnetic resonance EPR, and ferromagnetic resonance, FMR), excited nuclear states (by observation of perturbations in angular correlation of gamma-rays, PAC) and later also muon spins (muon spin relaxation, MuSR), from which other examples are selected.

1 Introduction

The present article is written to commemorate the invention, 75 years ago, of spin-based methods for the study of internal dynamics in molecules and solids and to show how these methods have developed up to the present time. Any attempt at a comprehensive account of all the variations and spin-offs of these initial methods would clearly be an impossible task since many thousands of scientists have worked in the field over the years and the literature produced up to now would fill whole libraries. Therefore, the progress is illustrated by means of selected examples, showing the great variety of problems for which spin interactions have given very detailed—and most often unique—information on important physical, chemical (and now also biological) processes. Overviews exist already for the most common spin-based methods (for instance [1] covering 50 years of NMR), but an ambition is here to include examples also from several other of the less well-known methods based on spin-interactions.

After a short overview of the development of the spin concept and its first experimental manifestations, some basic concepts common to all the methods discussed here are introduced; they will provide a basis for the presentations in the examples which follow. Examples are taken from different stages of methodological development; from the first tentative attempts up to advanced studies of topics of recent interest. It cannot be avoided that such a selection reflects the author's personal preferences, but the aim has been to present contributions from most of the quite different fields where spin-based methods have given specific and unique information. Considering the immense activities in the relevant areas, these examples can only be short glimpses from a class of spectroscopies which now have reached a considerable age but are still flourishing and continuously developing.

[a] e-mail: erik.karlsson@physics.uu.se (corresponding author)

2 Brief history of spin-based spectroscopies

2.1 Angular momentum of atomic particles

Angular momentum is produced by orbital motion of particles as well as by rotation of particles around their own axes (spinning). In classical physics, a particle with mass m and charge e rotating in a circle with radius r produces an angular momentum $l = mv \times r$ and a magnetic moment $\mu = (e/2m) \times l$. These relations are used to define the Bohr magneton $\mu_B = e\hbar/2m_e$ and nuclear magneton $\mu_N = e\hbar/2m_p$ as units of electronic and nuclear magnetism, where the magnitude of angular momentum is expressed in terms of $\hbar = h/2\pi$ and m_e and m_p are the electron and proton masses, respectively. The magnetic moment of a spinning classical particle depends on its internal charge distribution which requires integration of moving charges over its volume.

The quantization of angular momentum in terms if integer values of $\hbar$ was one of main propositions in the "old" quantum theory (see ter Haar [2] for an overview). But when Alfred Landé interpreted line splittings in atomic spectra in terms of energy states expecting them to be produced by valence electron interactions there was a hitch. To fit the data from the so-called anomalous Zeeman-effect [3] he had to introduce "atomic rest"-terms for the angular momentum, thought to arise from core electrons. He claimed [4] that such terms must have fractional values $(1/2)\hbar$, $(3/2)\hbar$, etc., not allowed by the old quantum theory, and that the $(1/2)\hbar$-term must be associated with one unit of μ_B, i.e., having a gyromagnetic ratio of magnitude $|g| = 2$.

2.2 Intrinsic spins of elementary particles

The concept of electron spin goes back to Samuel Goudsmit and George Uhlenbeck, who in the autumn of 1925 [5,6] proposed that electrons carry a property not described before, an *intrinsic* angular momentum, a spin of size $(1/2)\hbar$. This was an alternative interpretation of Landé's "atomic rest"-factor (it had actually been suggested, but unpublished, earlier by Ralph Kronig, one of Landé's assistants).

Wolfgang Pauli first criticized this idea since the electron's surface (in the prevailing picture) would in such a case be moving faster than the speed of light to produce the necessary angular momentum. But he changed his mind, admitting that the electron spin had no classical counterpart, and realized that its introduction was equivalent to his proposal of "two-valuedness" of electrons [7], a concept he used soon after [8] to explain particles' statistical properties, later known as the "Pauli principle," one of the corner stones of quantum physics. He formalized a theory for spins by introducing the Pauli spin matrices.

Pauli's introduction of the spin in quantum mechanics was still made "ad hoc," but in 1928 it appeared in a general framework when Paul Dirac [9] introduced his relativistic quantum mechanics which led to four-spinor wavefunctions. The spinor functions were interpreted as representing particles and antiparticles, each of them having spins "up" and spins "down." Dirac's relativistic theory also led to the gyromagnetic ratio $g = -2$ for the magnetism associated with the intrinsic spin of the negatively charged electron. By that, the theoretical basis for the spin concept and its associated magnetism was firmly established. Later, small corrections to this value were introduced by quantum field theory, giving $g_e = -2.00231930436256(35)$ and $g_\mu = -2.0023318418(13)$ for the electron and muon gyromagnetic ratio, respectively. In the following, intrinsic spin is denoted by $\mathbf{S}$, orbital electronic angular momentum by $\mathbf{L}$, its vector sum $\mathbf{J} = \mathbf{L} + \mathbf{S}$, the nuclear "spin" (see below) by $\mathbf{I}$ and their sum $\mathbf{F} = \mathbf{J} + \mathbf{I}$, as conventional.

2.3 The first experiments involving spins

2.3.1 Electron spins

At this stage there existed already an experimental indication of the double nature of atomic states through the Stern–Gerlach experiment, which had shown in 1922 that a beam of silver atoms was split into two after passing an inhomogeneous magnetic field [10]. This experiment was conceived and interpreted as a test of space separation of charged states, but the correct interpretation in terms of electron spins (assumed to have an associated magnetic moment, and therefore experiencing different net deviating forces for spins "up" and "down" when traveling in an inhomogeneous field) came in 1927 through Phipps' and Taylor's experiment with hydrogen atoms [11].

In Stern–Gerlach type of experiments, Frisch and Segré [12] later observed transitions between sublevels of the electron angular momentum $\mathbf{J}$ when the atoms were allowed to travel further into an additional homogeneous magnetic field. Isidor Rabi pointed out [13] that the same method could be used to study transitions between nuclear spin states $\mathbf{I}$ via the interaction $\mathrm{H} = a\,\mathbf{I} \cdot \mathbf{J}$, now understood to be the reason for the hyperfine splitting seen in optical spectra by Albert Abraham Michelson already in 1881 (for a review, see Shankland, [14]).
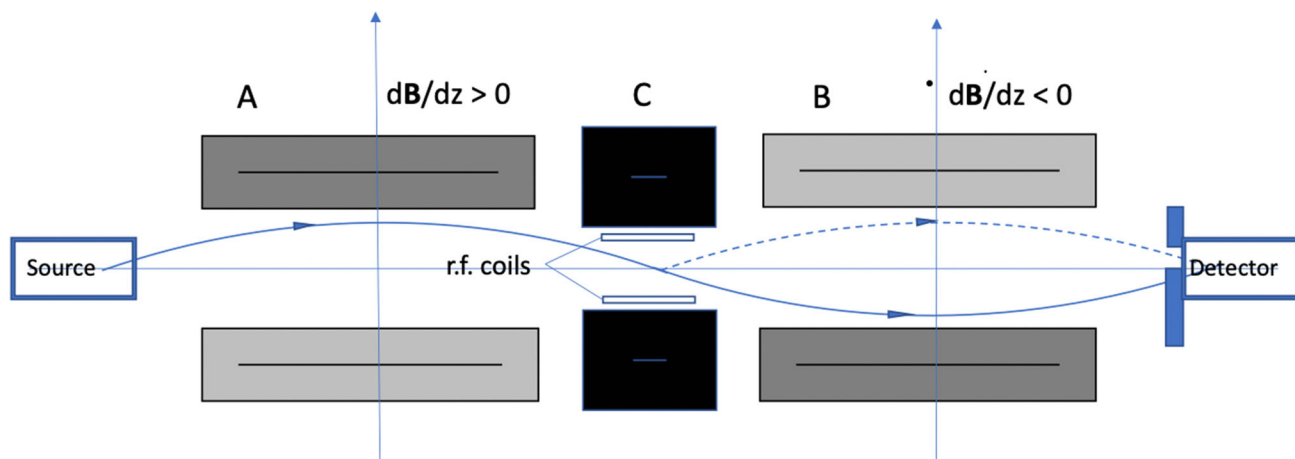
Fig. 1 Rabi's arrangement for spin resonance. Magnet C produces the field B_{ext}

2.3.2 Nuclear spins

Although atomic nuclei are composite particles whose angular momenta and magnetic moments are made up both by intrinsic spins and motions of their constituent protons and neutrons (including collective rotational or vibrational motions of all of them), their angular momenta are still conventionally described as "nuclear spins."

The first measurements of nuclear spins and their associated magnetic moments were made by Hans Kopfermann in 1933 [15]. He analyzed hyperfine splittings in optical spectra and determined the spins $I = 5/2$ and $I = 3/2$ for the rubidium isotopes ^{85}Ru and ^{87}Ru. To estimate their associated magnetic moments from the energy splittings he used Fermi's calculation of the so-called contact field $B_s(0)$ produced by s-electrons at the nuclear sites, published in 1930 [16]. The results for the magnetic moments were 1.4 μ_N and 2.8 μ_N (modern values from nuclear resonance are 1.35267(3) μ_N and 2.75050(6) μ_N, respectively [17]).

2.3.3 Resonance techniques and NMR

In the 1930's, Isidor Rabi and his colleagues developed a two-step Stern–Gerlach arrangement (Fig. 1), where transitions between different nuclear spin states could be introduced during the passage between two (oppositely arranged) inhomogeneous magnetic field regions by application of a radio-frequency field with photon energy $E_{\text{rf}} = h\nu$ in the presence of a static magnetic field B_{ext}. When E_{rf} was equal to the energy difference $\Delta E_N = \mu_N g_N B_{\text{ext}} \Delta M_I$ between levels with nuclear spin components M_I, the spins were flipped and a resonance could be detected by observing changes in the outgoing atomic or molecular beams.

Nuclear resonances were measured by Rabi and collaborators in 1938 [18] using LiCl molecules which have an electron cloud with $J = 0$ meaning that the nuclear spins of Li^7 and Cl^{34} and Cl^{38} were the only angular momenta present (neglecting small contributions from molecular rotation). The result for Cl^{34} was $\mu_I = g_N I_N \mu_N = 3.250$ μ_N. Several nuclear magnetic moments were determined by this method, but later research based on the Rabi method was more focused on spectroscopy of molecules, in which several spins interplay and produce a more complicated set of peaks in the radio-frequency spectrum. In the measurements of H_2, D_2, and HD [19] there were several magnetic interactions in addition to that of the $\mathbf{I} \cdot \mathbf{B}_{\text{ext}}$-terms: molecular rotation ($\mathbf{K}$) interacting with $\mathbf{B}_{\text{ext}}$, interaction $\mathbf{K} \cdot \mathbf{I}$ between $\mathbf{I}$ and $\mathbf{K}$ and interaction $\mathbf{I}_1 \cdot \mathbf{I}_2$ between different nuclei, splitting the resonances. In the present perspective, these experiments can be seen as the first use nuclear spin methods to get information on a nuclear environment.

In contrast to atomic beam experiments in gases, initial spin states cannot easily be selected in liquids or gases before resonances are induced. Therefore, standard nuclear resonance experiments on condensed systems must rely on the small excess population of nuclear M_I-states appearing when they are placed in magnetic fields. It follows the Boltzmann distribution $P(M_I) \approx \exp(-E_M/kT)$, i.e., approximately as $P(M_I) = 1 + \mu_N g_N B_{\text{ext}} M_I / kT$ for high temperatures. The population differences are small; at room temperature around $\Delta P(M_I) \approx 10^{-6}$ for $\Delta M_I = \pm 1$ at typical magnetic fields (1 T). This population of partially oriented nuclei carries a magnetic moment $\mathbf{M}$ and a total angular momentum $< \mathbf{I} >$. Another limitation for resonance experiments in condensed media was that lines were broadened because of strong perturbations by internal interactions (but some degree of spin coupling to the environment is necessary for reaching the thermalized states in the applied magnetic field).

In 1945, with the advent of more powerful radio-frequency sources developed during the second world war, two research groups tried to see spin resonances for nuclei in liquids. Practically simultaneously, the groups led by
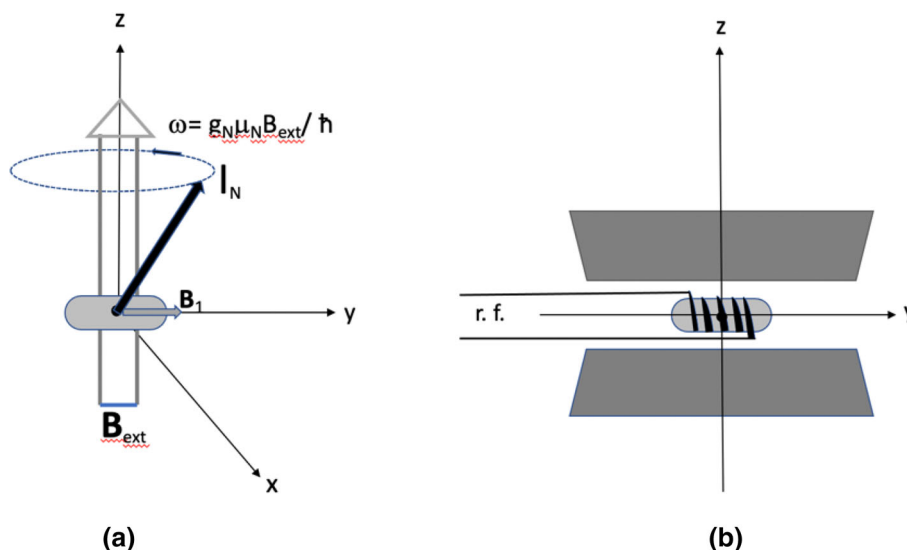
Fig. 2 **a** Larmor precession of a nuclear spin I_N in B_{ext}, **b** in Purcell's method, the same r.f. coil (along y) can be used both for exciting the resonance and for detecting absorption; Bloch had a separate coil for detection

Edward Purcell at MIT [20] and by Felix Bloch at Harvard University [21], reported successful observation of resonances. These two groups were working independently and of different detection techniques.

Both methods observed the magnetization **M** of a large number ($>> 10^6$) nuclei, polarized in an external field $\mathbf{B}_{ext}$. The angular momentum of $< \mathbf{I} >$ of these nuclei is changed at the rate $d < \mathbf{I} > /dt = \mathbf{M} \times \mathbf{B}_{ext}$ which leads to a <u>Larmor precession</u> [22] with angular frequency $\omega_L = (g_N \mu_N/\hbar) \times B_{ext}$ of **M** around $\mathbf{B}_{ext}$ (the z-axis), as illustrated in Fig. 2a. The factor $(g_N \mu_N/\hbar)$ is conventionally written as γ_N.

In nuclear magnetic resonance (NMR), a weak oscillating field $\mathbf{B}_1$ applied perpendicular to $\mathbf{B}_{ext}$ turns the **M**-vector down from the z-axis so that it lies in the x–y-plane at resonance. The resonance was detected by Purcell [20] as an energy absorption in the oscillating field coil (as seen by comparing it with a dummy coil + sample in zero external field) and by Bloch [21] as a maximum in the induced voltage in a coil lying along the y-axis (Fig. 2b). At resonance the absorbed energy is $\Delta E = \hbar\omega = \mu_N g_N B_{ext}\Delta M_I$ per nucleus. Purcell found the resonance by varying ω at constant B_{ext} and Bloch by varying B_{ext} at constant ω.

The first NMR-spectrometers worked with continuous r.f. fields, but already in 1950 Erwin Hahn [23] used <u>pulsed NMR techniques</u> in which the duration t of the r.f. pulse is chosen such that **M** is turned 90 degrees (a $\pi/2$ pulse). After such a pulse, the magnetization continues to precess freely in the (x, y)-plane if not perturbed by other disturbing fields (called Free Induction Decay, FID). Hahn also showed how a second 180 degree pulse applied after a certain time interval τ can be used to produce a "spin-echo" (for details, see Sect. 3.3).

The action of the r.f. field $\mathbf{B}_1$ is usually illustrated in a coordinate system S' which rotates around the z-axis with the Larmor frequency ω_L (Fig. 3a): here an oscillating field along y' turns the magnetization **M** around the y'-axis with frequency ω (slowly, since $\omega << \omega_L$).

In the absence of all other spin interactions, the FID would be a single frequency, undamped oscillation, but weak local fields at different nuclear positions in molecules or solids split the resonances. This is illustrated in Fig. 4 for a hypothetical molecule with two nuclei of the same kind sensing different local fields from dipoles in their vicinity. There will be two close-lying resonance peaks and a FID-signal which is a superposition of two frequencies.

Each of these FID-components will have its own characteristic damping caused by spreads in local fields or different fluctuations in the molecule. FID's are time-Fourier transforms of the frequency spectrum F(ω) and vice versa.

By 1961, Ernst and Anderson [24] had developed pulsed NMR spectroscopy to a high degree of perfection. Figure 5 on page 6 (from Ref. [25]) shows the FID-signal for an organic molecule with several protons resonating at different frequencies. The Fourier transform spectrum (FT) revealed many more details than could be achieved in the continuous wave (CW) spectroscopy used before.

NMR-spectroscopy was further developed after Jeener's proposal in 1967 [26] to use simultaneous excitation, so-called coincidence spectroscopy (COSY), of two nuclei at different positions in a molecule, having different chemical shifts and responding to different frequencies. Figure 6 on page 6 shows a 2D-NMR contour plot obtained in 1979 by Jeener, Meier, Bachmann and Ernst of proton resonances in the heptamethylbenzenomium ion [27].

Except for the resonances at the diagonal positions in this diagram there are non-diagonal elements showing that the proton at position A interacts with the one at C, and the one at B interacts with the ones at C and
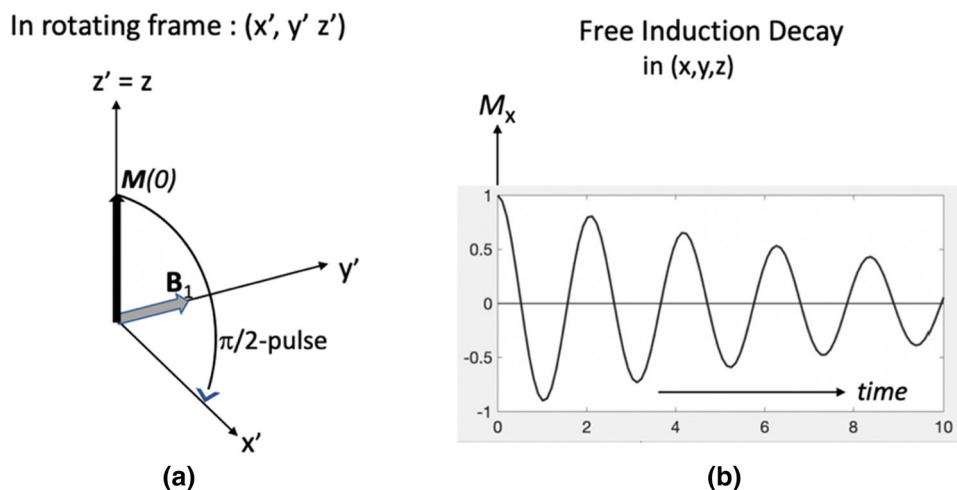
Fig. 3 a A short B_1 pulse (at frequency ω) turns the nuclear magnetization $\boldsymbol{M}$ down to the x'-axis in the system (x', y', z'), which rotates around $(z' = z)$ with the Larmor frequency, **b** Thereafter, a pick-up coil (along x in the fixed system) registers an oscillating signal, the FID, when $\boldsymbol{M}$ rotates in the $x-y$ plane
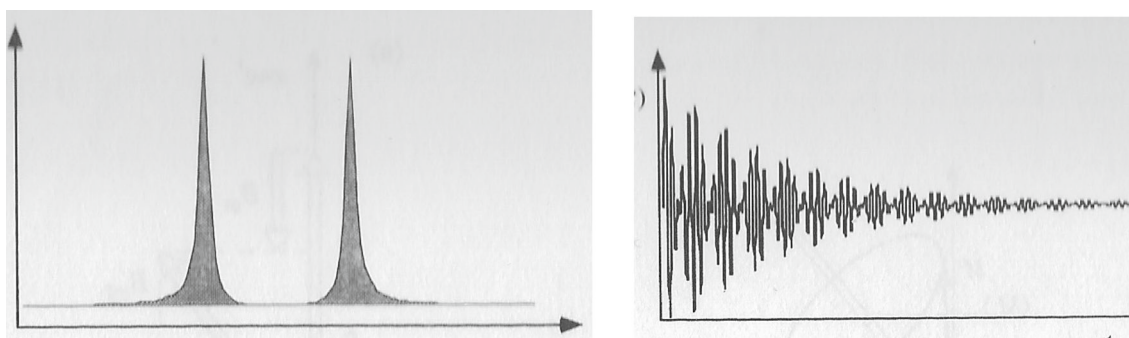

Fig. 4 Split resonances, with Fourier transform (FID)

D. By applying appropriate pulse sequences, 2D-NMR spectra can be used to derive information on one proton's relative position in the molecule to another one (through their anisotropic dipolar interactions) as well as their spin relaxations.

Further development involves coincidence spectroscopy with pairs of <u>different</u> nuclei, for instance (^{1}H, ^{15}N) or (^{1}H, ^{13}C), to be exemplified later, and extensions to 3D-NMR (and even 4D, displaying time correlations [28,29]).

2.3.4 Other spin-based methods

Figure 3 serves also as a starting point for description of the other spin-based methods to be described in the following text. <u>PAC (Perturbed Angular Correlation)</u> studies the magnetic interactions in *excited nuclear states* observed in gamma–gamma cascades (γ_1, γ_2) during radioactive decay. A subset of M_I's is selected by the detection of γ_1 in a certain direction, which leads to a directional correlation of the γ_2 emission with respect to that of γ_1. In a field $\mathbf{B}_{\mathrm{ext}}$ perpendicular to the (γ_1, γ_2) plane, the γ_2-radiation pattern rotates with $\omega_{\mathrm{L}} = (g_N \mu_N / \hbar) B_{\mathrm{ext}} = \gamma_N B_{\mathrm{ext}}$, like the FID in NMR.

In <u>MuSR (Muon Spin Rotation)</u>, a positive muon is implanted into the material to be studied.

Muons are strongly spin polarized along their implantation direction, which serves as a reference direction for their precession in an external $\mathbf{B}_{\mathrm{ext}}$ or in internal fields $\mathbf{B}_{\mathrm{int}}$ present in magnetic materials. By the free choice of the initial spin direction with respect to crystalline axes it offers a unique possibility to choose starting conditions for spin precession or spin relaxation measurements in crystalline matter. PAC- and MuSR-spectra are studied both in the time domain and as Fourier transforms. Standard NMR can also be combined with specific selection techniques to increase sensitivity, such as registering it in combination with a nuclear decay which selects certain spin substates [30] or by optical detection of the resonances [31].

<u>Electron spin resonance</u> (ESR) also called electron paramagnetic resonance (EPR) works with unpaired spins which are found in ions with partly filled electronic shell (transition elements), in molecules having an odd number of electrons, and more rarely in molecules with an even number of electrons but a resultant angular momentum
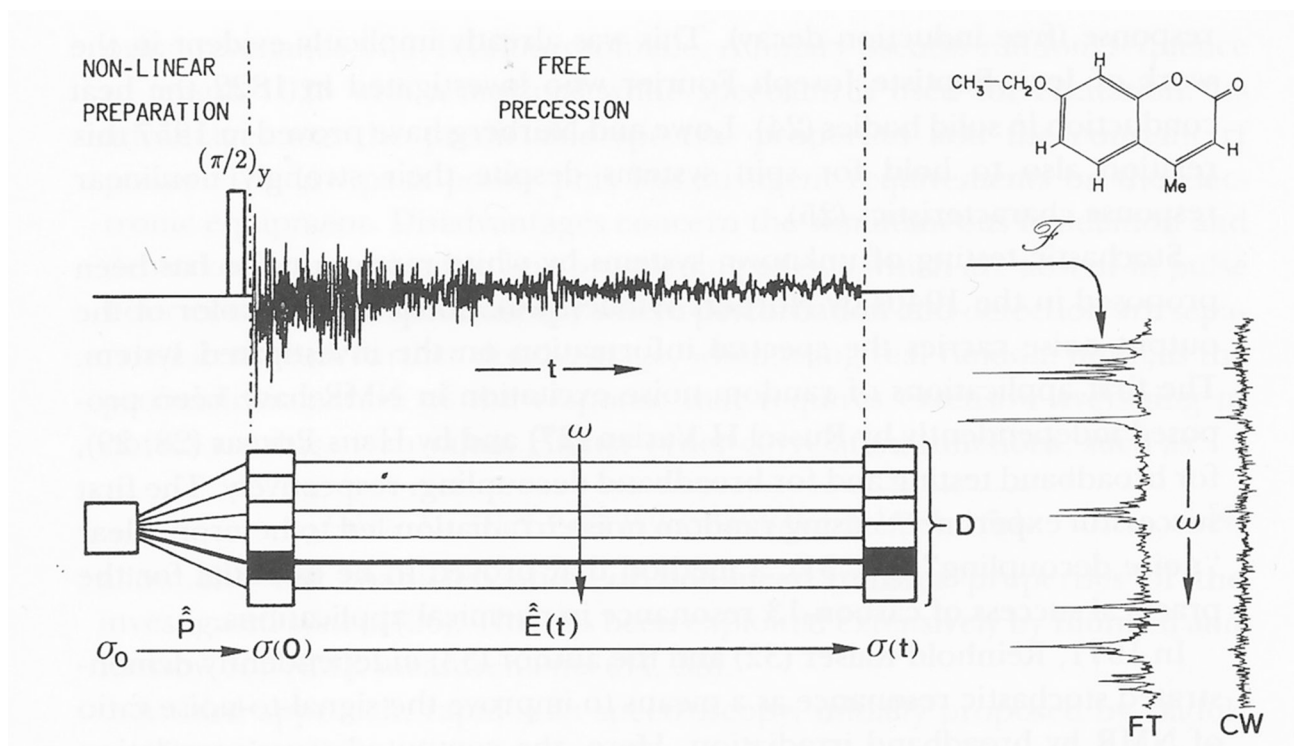
Fig. 5 FID from protons in the molecule 7-ethoxy-4-methyl-coumarin, Fourier transformed to derive F(ω). To the right: comparison to CW-NMR [25]
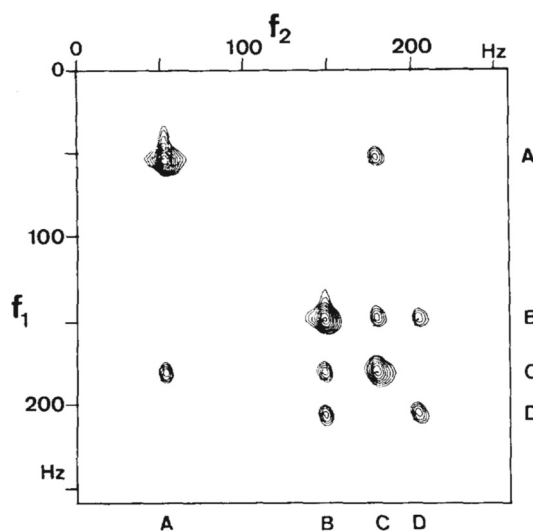

Fig. 6 2D exchange spectrum of protons in the heptamethylbenzenomium ion. Isotope shifts f fall in the 0–250 Hz range. From [27]

(such as O_2), and also in free radicals. The first electron spin resonance is actually 1 year older than NMR. It was performed by Zavoisky [32], who induced transitions between Zeeman levels of copper chlorides and sulfates by microwaves, and published it in 1945.

The energy splittings of the $M_S = +1/2$ and $M_s = -1/2$ levels equal to $g_e\mu_B B_{ext}$, which in typical external fields of 0.35 T corresponds to resonance frequencies of 10 GHz, i.e., about 1000 times higher than in NMR. Resonance lines are split by into $2M_I + 1$ multiplets through interaction with the associated nuclei. EPR in solids was used early for determination of energy splittings and magnetic properties of transition element ions in different crystal fields (see Bleaney and Stevens, 1953 [33]) and has later become a rich source of information on color centers and defects in crystals [34].

Ferromagnetic resonance (FMR) is used to study magnets and antiferromagnets where electron spins are ordered with a bulk magnetization $\mathbf{M}_S$. An applied magnetic field splits the $M_S = +1/2$ and $M_S = -1/2$ levels of the individual spins and the magnetization precesses with the Larmor frequency $\omega_L = (g\mu_B/\hbar)B_{\text{eff}}$, where $\mathbf{B}_{\text{eff}} = \mathbf{B}_{\text{ext}} + \mathbf{B}_{\text{dem}}$ (demagnetizing field, dependent on sample shape) $+ \mathbf{B}_{\text{anis}}$ (magnetocrystalline anisotropy field). Resonances appear in the 10 GHz range for typical magnets. They are damped out by various viscous processes, including two-magnon scattering.

Spectra from the different spin-based spectroscopies are rich sources of information on internal structure of molecules and solids but the present text will be limited to studies of dynamical processes only. Likewise, most experiments based on the *electric interaction* between the nuclear quadrupole moment Q and electric field gradients V_{zz} (which appear for $I \geq 1$) will be left out for brevity.

Magnetic and electric fields from surrounding nuclei or electrons perturb the Larmor precession. They cause a damping in the FID-oscillations and a corresponding smearing out of the resonances, particularly in dense solid or liquid systems. But once understood and with the observed perturbations correctly interpreted they form a rich source of information for all kinds of internal dynamics in liquids and solids, as will be presented in the examples below.

3 Spin relaxation

3.1 Definitions

Although first considered as a limitation for the exact measurement of nuclear magnetic moments, it was immediately realized by the NMR pioneers that spin perturbations might contain information about the immediate environment of the resonant nuclei. They introduced the concept of *spin relaxation* for the gradual loss of the spin orientation in the static field B_{ext} and distinguished between *spin–lattice* and *spin–spin relaxation*. Felix Bloch wrote in 1946 [35]:

"It was shown in Sect. 4 that the induced signals to be expected depend not only upon the nuclear susceptibility but also upon the relaxation times. By suitable choice of the variation with time of the resonant field or frequency, it is thus possible to measure these quantities separately. The study of nuclear relaxation times is of interest not only as an experimental method to investigate the establishment of thermal equilibrium, but also because of its importance for reaching extremely low temperatures through the nuclear calorimetric effect. While even the information gained at room temperature is valuable, it is clear that it can be greatly enlarged by studying the temperature dependence of the effect and particularly its behavior at low temperatures. It is in this same respect that the effect of paramagnetic catalysts, mentioned in Sects. 1 and 4, seems of considerable interest."

Bloch also introduced phenomenological equations for the changes of the components of nuclear magnetization $\mathbf{M}$:

$$\mathrm{d}M_z/\mathrm{d}t = -(M_0 - M_z)/T_1 \; ; \quad \mathrm{d}M_x/\mathrm{d}t = -M_x/T_2; \quad \mathrm{d}M_y/\mathrm{d}t = -M_y/T_2 \tag{1}$$

where M_0 is the initial magnetization (along the z-axis) and T_1 is the *longitudinal relaxation time* and T_2 the *transverse relaxation time*. T_1-relaxation was called "spin–lattice"-relaxation because one major reason for it was the lattice vibrations of surrounding atoms and T_2 "spin–spin"-relaxation because interactions between nearby spins tend to destroy the phase coherence in the Larmor precession of the participating nuclei, therefore reducing the macroscopic M_x and M_y components.

For deriving kinematic properties of the nuclear environments from measured T_1 and T_2 values it is necessary to have a description of the different mechanisms which cause the relaxations. The determination of T_1 is straightforward but the origin of the T_2 term in Eq. (1) must first be clarified. It has two different reasons. One has to do with the homogeneity of the internal fields $\mathbf{B}_{\text{int}}$ experienced by the nuclei; if it is not the same for all individual nuclei in the sample, they will precess with different frequencies ω_L. The other reason is interaction with other static or fluctuating nuclear or atomic spins, which is a source of information about environmental fluctuations of interest here. The rate can be expressed as,

$$1/T_2 = (1/T_2^\Delta) + (1/T_2^*) \tag{2}$$

where T_2^Δ comes from the field inhomogeneity $\Delta\mathbf{B}_{\text{int}}$ and T_2^* from the environmental interactions.

The inhomogeneity $\Delta\mathbf{B}_{\text{int}}$ can have the trivial reason that the applied field $\Delta\mathbf{B}_{\text{ext}}$ is not perfect enough, but arises also from the magnetic dipole moments μ_i of nearest surrounding nuclei at positions r_i, θ_i (Fig. 7a) These have almost random spin directions (in the B_{ext}'s applied at normal temperatures) and cause a distribution in the

(a)   **(b)**
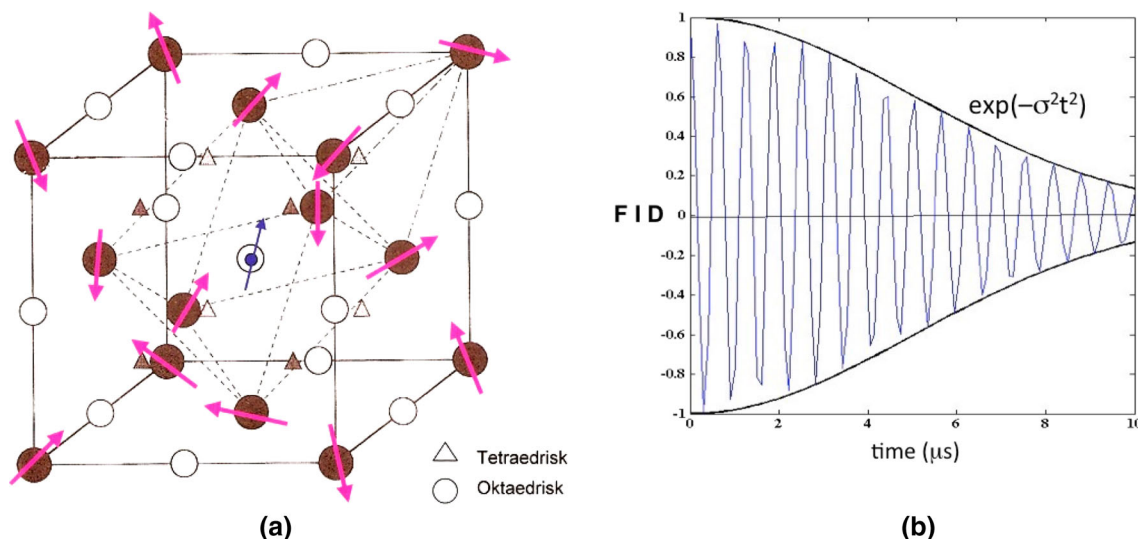
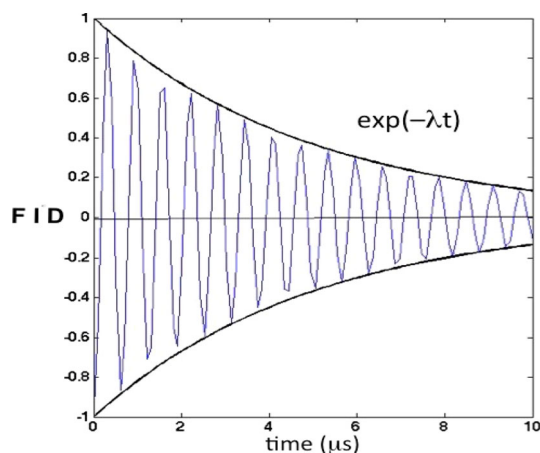**Fig. 7** **a** Nuclear dipoles surrounding a probe spin, **b** Gaussian damping of spin precession

Fig. 8 Lorentzian damping

field felt by the studied spins whose average square (second moment) is

$$< \Delta B_{\mathrm{dip}}^2 >= (1/3)(g_I \mu_N)^2 I(I+1) \Sigma_i (1 - \cos^2 \theta_i)^2 / r_i^6. \tag{3}$$

At each nuclear position, there is a different dipole field $B_{\mathrm{dip},i}$ which tends to turn its spin $\mathbf{I}_i$ an angle proportional to $\gamma\, B_{\mathrm{dip},i} \times t$, the square of which averages to $\gamma^2 < \Delta B_{\mathrm{dip}} >^2 t^2 = \sigma^2 t^2$ for the nuclear ensemble. This leads a damping of the external field precession $\cos(\omega_L t)$ by the Gaussian-type factor $\exp(-\sigma^2 t^2)$, as illustrated in Fig. 7b.

This time-development of the signal can be changed for two different reasons:

(1) the studied nuclei are mobile (like the interstitial atom in the center of Fig. 6),
(2) the neighboring nuclear spins fluctuate strongly, averaging out the dipole fields.

In the first case, the motion can be described as a random walk (self-diffusion in a lattice), where an average distance x is reached after n steps of length d. It obeys the relation $< x^2 > \approx d^2 \times n$, where n is the number of steps. Likewise, spins diffusing between different positions are exposed to $n = t/\tau_c$ random rotation steps of size $\omega_{\mathrm{dip}} \times \tau_c$ over a time t. This results in an average $< \omega_{\mathrm{dip}}^2 \tau_c^2 > \approx \omega_{\mathrm{dip}} \tau_c \times n = \omega_{\mathrm{dip}} \times \tau_c t$, where τ_c is the characteristic correlation time for staying in each position. For fast diffusion the spin precession in $\mathbf{B}_{\mathrm{ext}}$ is damped by a Lorentzian function $\exp(-\lambda t)$, where $\lambda = \sigma^2 \tau_c$. The same is valid for a non-diffusing particle when the spin directions of the neighboring nuclear fluctuate strongly, as in liquids where molecules tumble or rotate. These motional-narrowing expressions satisfy the Bloch equations and make T_1 and $T_2{}^*$ well defined (Fig. 8).

3.2 Theories connecting T_1 and T_2* with internal motions

Bloembergen, Purcell and Pound [36] formalized the fluctuation theory and described the time developments $f(t)$ of the dipole interactions in terms of their autocorrelation functions $G(\tau) = f(t)f(t')$, where $\tau = t' - t$. The autocorrelation function tells to what extent $f(t)$ can be predicted (on the average) by its value $f(t - \tau)$, τ seconds earlier. The function $J(\omega)$ is the Fourier transform of $G(\tau)$ and for fast fluctuations, where $J(\omega)$ contains components at $\omega = \omega_L$ (and at $\omega = 2\omega_L$), it can induce M_{Iz}-transitions (T_1-relaxation) and M_{Ix} or M_{Iy} -transitions (T_2*-relaxation) by flipping individual spins $\mathbf{I}_I$. Abragam [37] provided detailed relations between relaxation rates $(1/T_1)$ and $(1/T_2^*)$ and fluctuation parameters for different interacting objects surrounding the spin $\mathbf{I}_I$:

(a) other nuclear spins (of the same kind or of a different kind)
(b) paramagnetic impurities
(c) conduction electrons
(d) phonons (mainly interacting through Raman scattering, where the Raman shift $\omega - \omega' = \omega_L$).

They allow the determination of different internal parameters in the samples from the relaxation rates: molecular rotation and translation, viscosity in liquids, spin correlations in magnets and phonon and magnon modes. If the fluctuations are <u>fully random</u>, the equations are simplified; if all correlation functions have an exponential decay, $\exp(-t/\tau_c)$—which can be motivated for instance for fast Brownian motion—the function $J(\omega)$ can be expressed as

$$J(\omega) = 2\tau_c/(1 + \omega^2/\tau_c^2) \tag{4}$$

where τ_c is the characteristic correlation time for the fluctuation. $J(\omega)$ has its maximum when $\tau_c = 1/\omega$. A fluctuating magnetic field $\mathbf{B}_{loc}$ at a nuclear site originating from surrounding spins fluctuating with correlation time τ_c gives rise to a T_1 relaxation rate

$$1/T_1 = 2(g_I\mu_N/\hbar)^2(B_{loc}^2/3)\tau_c/(1 + \omega^2/\tau_c^2) \tag{5}$$

Equations (4) and (5) are valid when the surrounding spins are different from the one at the site considered (a correction factor 3/2 applies for equal spins). The $(1/T_2^*)$-rate coincides with that of $(1/T_1)$ for short τ_c but continues to increase linearly for long τ_c (cf. Fig. 10 later in this text).

For non-magnetic materials, the dipolar field $\mathbf{B}_{dip}$, produced by nearby nuclear magnetic moments is of the order of 0.01 T, but with unpaired electronic spins present $\mathbf{B}_{loc}$ can amount to 0.1–1 T. With B_{loc} known from other sources, very short correlation times τ_c (down to 10^{-13} s) can be derived from the measured T_1's or T_2*'s.

3.3 Spin-echo techniques

If in pulsed NMR, the $\pi/2$ pulse in Fig. 3a is followed after time τ by a π pulse (turning the each spin 180 degrees in the x, y plane), the phase differences for the individual precessing nuclei caused by the ΔB_{int}-differences will be compensated after time 2τ, because the inversion of spins is equivalent to inversion of time in the precession process. A *spin echo* peak in the M_x or M_y signal appears after the time $t_E = 2\tau$ when all phase differences are restored, as first observed by Hahn in [23] and soon thereafter described in more detail by Carr and Purcell [38]. Its amplitude reflects the decay $\exp(-t/T_2^*)$ (Fig. 9).
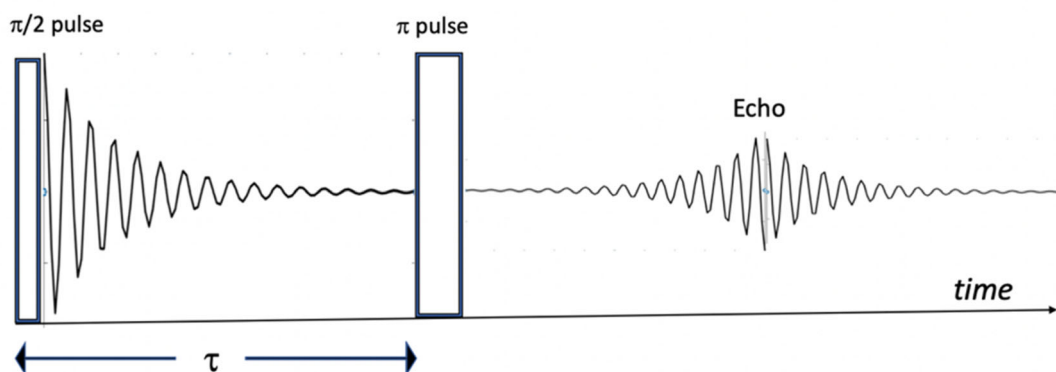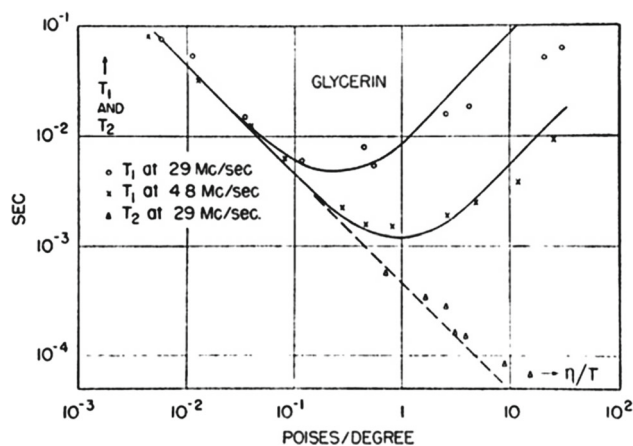

Fig. 9 Principles of the spin-echo technique

Fig. 10 T_1 (circles and crosses) and T_2 relaxation times (triangles) as function of η/T, measured by Bloembergen et al. [36]

This technique eliminates the inhomogenous contributions to T_2 and is extensively used to measure $T_2{}^*$ relaxation. It is an important element in the medical application MRI (magnetic resonance imaging).

4 Internal dynamics, studied by NMR

4.1 Examples

4.1.1 First information from NMR-relaxation

The paper by Bloembergen, Purcell and Pound [36], published only 1 year after the invention of NMR contained already the main elements of the theory behind spin relaxation. They studied protons in water (viscosity η), where random rotations of the molecule with size a, give an estimated correlation time of

$$\tau_c = 4\pi\, a^3 \eta/3kT). \tag{6}$$

At $T = 20$ C, it was expected to give $T_1 = 1.9$ s, via the dipolar interaction $\gamma_N \hbar B_{\mathrm{dip}}$, when one proton spin rotates with respect to another. The measured value was $T_1 = 2.3$ s; the small discrepancy was assigned to influences of intermolecular spins (recent measured values for T_1 in water are closer to 4 s). They also measured T_1 and T_2 for glycerine at different viscosities η where the measured data (Fig. 10) verified Eq. (6), assuming that τ_c is proportional to η/T .

4.1.2 CH_3 rotation by tunneling

CH_3 groups are important constituents of many organic molecules. In 1955, Powles and Gutowsky measured NMR relaxation in three different molecules [39] in order to determine whether their rotation (Fig. 11, 12) could be described as classical or as a quantum tunneling of the three protons involved. Measurement of T_1 as function of temperature yielded correlation times τ_c whose T-dependences could be expressed by the Arrhenius relation

$\tau_c = \tau_0 \times \exp{(E_a/RT)}$, where $\tau_0 = 1/\nu_0$ is the frequency factor and E_a the activation energy for the hindered rotation. The ν_0 values ($10^7 - 2 \times 10^8\,\mathrm{s}^{-1}$) as well as the activation energies ($E_a = 2.5$ kcal/mol) clearly favored the quantum tunneling process in a periodic potential, see Fig. 11, 12 (classical rate theory predicted an attempt frequency $\nu_0 = 2.7 \times 10^{12}\,\mathrm{s}^{-1}$ for rotation).

During the following decades, detailed methods for analysis of molecular motion were developed, as described in a textbook by H. W. Spiess [40] from 1978.

4.1.3 Magnetic resonance imaging, MRI

The idea that NMR relaxation times could be used to distinguish different kinds of living tissue (and changes in certain tissues caused by natural processes or illnesses) occurred to Erik Odeblad in 1957 and later to Raymond Damadian in 1971 [41]. Odeblad and Bryhn [42] studied secretions from human cervical mucus and saw differences
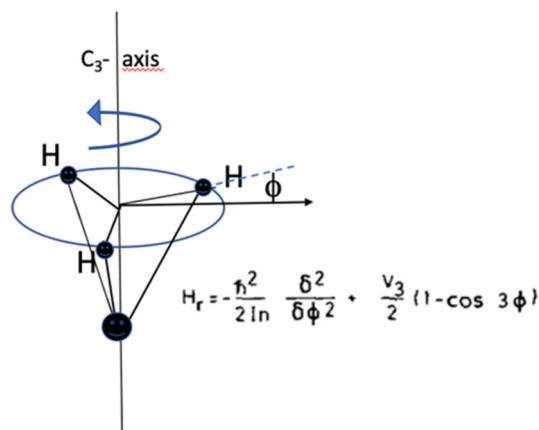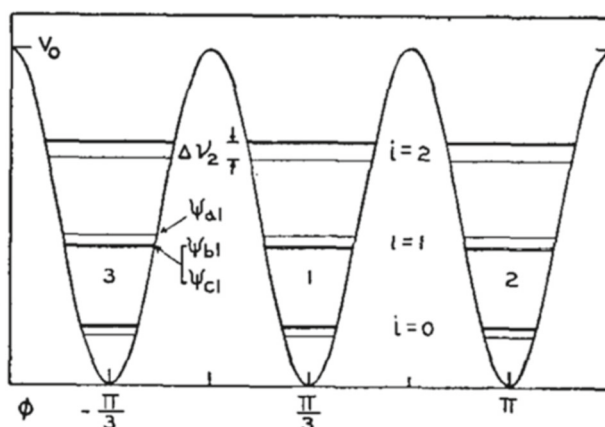
Fig. 11 Rotation of CH_3 groups

Fig. 12 The 3-fold potential with torsional oscillation levels and tunnel splittings [39]

**Table 1** T_1 and T_2 relaxation times in living tissue (at $B_{\text{ext}} = 1.5$ T)

Tissue type	T_1 (ms)	T_2 (ms)
Adipose tissues	240–250	60–80
Whole blood (deoxygenated)	1350	50
Whole blood (oxygenated)	1350	200
Cerebrospinal fluid ($\approx$ water)	4200–4500	2100–2300
Gray matter of cerebrum	920	100
White matter of cerebrum	780	90
Liver	490	40
Kidneys	650	60–75
Muscles	860–900	50

in T_1 during menstruation cycles and Damadian observed that tumors in rats containing malignant tissue had longer relaxation times than normal tissue.

NMR relaxation times in human tissue fall in the range 0.01–4 s (Table 1). Standard MRI does not search for the origin of these differences, but uses them to find the distribution of different tissues in a human or animal organ. It applies pulse sequences and scanner settings to increase contrast for a particular type of tissue, in so-called T_1 or T_2 weighted images. The more specific qMRI (quantitative MRI) is aimed at detailed measurement of T_1, T_2 and proton densities to compare with theoretical models and to aid in interpretation of signals from of a particular type of tissue.

To reach this goal it was necessary to make a series of NMR measurements over small area elements and combine the information into a 2D-picture. Paul C. Lauterbur first showed how this could be done in magnetic fields with gradients produced by shim coils [43]. With a gradient along the z-axis only, nuclei within a small Δz range

Fig. 13 Comparison between X-ray (left) and NRI images (T_1 in center, T_2 to the right) of human brain, cited in [44]
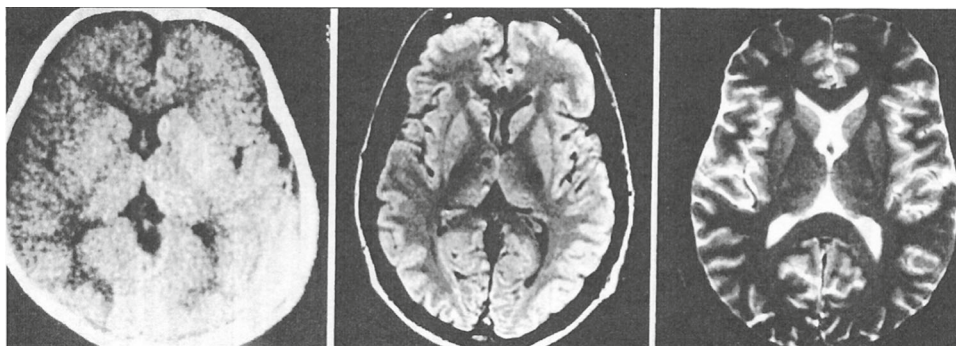
respond to the r.f. frequency applied, and similarly for gradients in x- or y-directions. With a stepped sequence of r.f. pulses and gradient pulses he showed how to produce 2D-pictures, whose elements contained information about proton density and proton relaxation. The book by Mattson and Simon [44] shows detailed pictures of the human brain obtained by T_1 and T_2 scans, compared to what can be sen by X rays (Fig. 13).

The nuclear resonance imaging (NRI) method, first called "zeugmatographic" (meaning "that which is used for joining") by Lauterbur, was further developed by Peter Mansfield. He worked out intricate r.f. and spin echo sequences and introduced EPI (echo planar imaging [45]) to improve selectivity and contrast in the images (which were now called MRI, magnetic resonance imaging, avoiding the scaring word "nuclear"). Referring back to original work by Ernst in 1966 [46], of fundamental importance for MRI, signal strength optimization is reached by flip pulses set at the "Ernst angle" $\theta_E = \arccos(e^{-(T_R/T_1)}$. For the long relaxation times T_1 often met in MRI, θ_E is considerably lower than the 90 degrees indicated in Fig. 9 at the typical repetition times T_R used.

The progress of this method was closely related to the simultaneous increase in data handling capacity. Its main information comes from spin relaxation, but to some extent also from local signal intensity, which maps proton density. Later MRI-techniques include "functional MRI" (showing activity in the brain) and "real time MRI" (for instance, following the motion of the heart). Other nuclear spins, e.g., ^{13}C, ^{23}Na and ^{31}P (naturally present in the body), can be used in MRI for specific purposes.

4.1.4 Hydrogen motion in metal hydride

Knowing hydrogen mobility in metals is important for the development of future hydrogen-based energy systems. When hydrogen is absorbed in metals, the protons take up interstitial positions in the lattice, as indicated in the center of Fig. 7a. At low temperatures the local field distribution gives rise to inhomogeneous broadening of the NMR resonance as described by Eq. (3) and Fig. 7b.

Because of its low mass, hydrogen diffuses easily (partly by quantum tunneling) to neighboring interstitial sites (Fig. 14a). During a random walk in the crystal lattice the proton spin is exposed to fluctuating local dipole fields, ΔB_{dip}. The FID-signal from static protons is damped by $\exp(-\sigma^2 t^2)$, but by $\exp(-\sigma^2 \tau_c t)$ if they diffuse with a short time of stay τ_c in each position. Random walk theory tells us that the distance covered after n jumps of length d is $< x > = 2d\sqrt{(n/2\pi)}$ and that τ_c is related to the classical diffusion coefficient by $D = (1/6) \ d^2/\tau_c)$. Figure 14b shows a typical temperature dependence. For intermediate temperatures correlation times τ_c can be extracted approximately using the interpolation formula $\exp \{-2\sigma^2 \tau_c^2 [\exp(-t/\tau_c) - 1 + t/\tau_c]\}$.

Figure 14c shows H-diffusion in Nb-hydride measured by Messer et al. [47]. Below room temperature Nb goes through two crystallographic phase transitions, $\beta \to \zeta$ and $\zeta \to \varepsilon$. The slopes of the lines give information about barriers for H-diffusion in each phase.

The study of Li-mobility in modern battery materials by NMR is an application of recent interest, as for example studied by Gray and Dupré [48].

4.1.5 Polymer dynamics

Research on structure and dynamics of polymers is fundamental for improvement of properties in all their different practical applications: plastics, textiles, conducting polymers and, lately, replacement of damaged human tissue by specifically designed polymers [49]. The most common investigation techniques are inelastic neutron scattering and NMR.

Polymers consist of chains, several μm long, of linked monomers (each about 10 nm). The different chains are intertwined in a complicated spaghetti-like manner. Edwards [50] introduced a "tube model," by which the essential features of chain motion and chain interactions could be described. Within such a tube, having a radius a, the molecular segments are supposed to move freely, except for local interactions with other chains at "entanglement" points. At such a point there appears a kink, which moves like a snake along the chain (Fig. 15). This motion
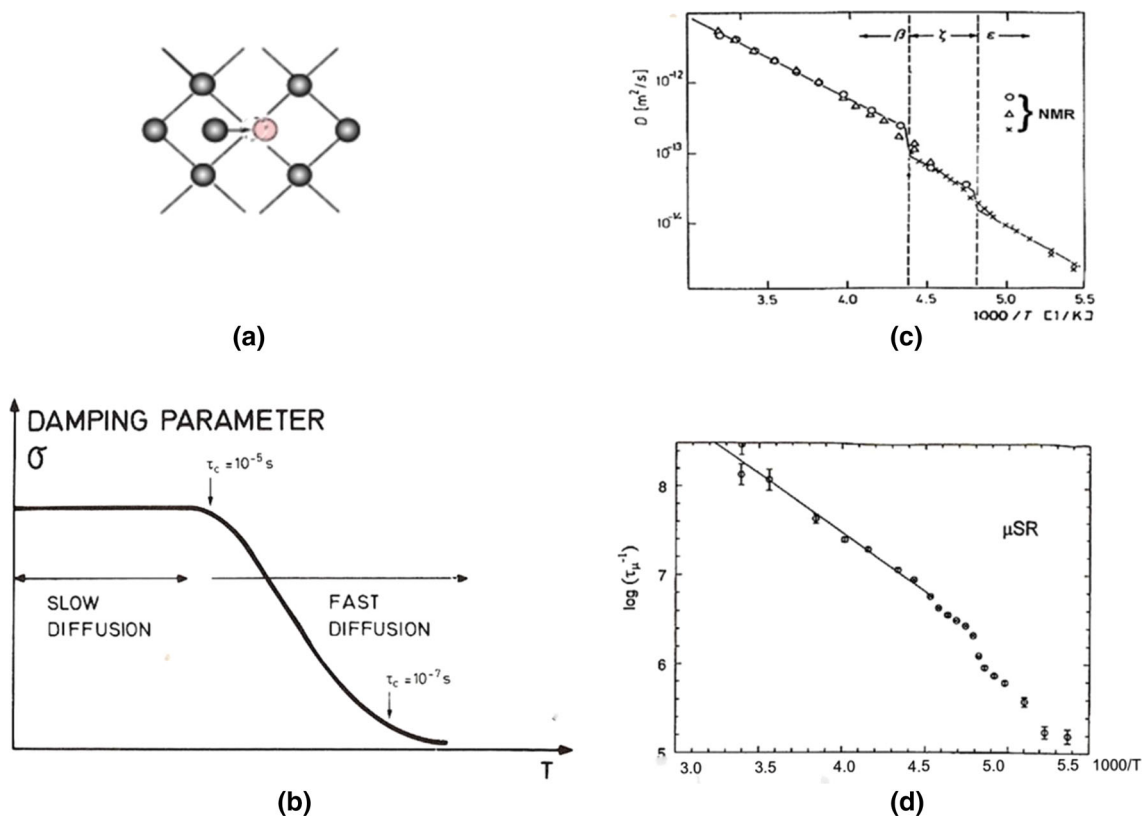
(a)

(c)

(b)

(d)

Fig. 14 H-motion in different crystallographic phases of Nb: **a** a single diffusion step, **b** damping of precession signal as function of temperature (τ_c-values valid for positive muon diffusion), **c** H-diffusion rates measured by NMR [47] and **d** μ^+ jump rates measured by MuSR (lower plot, to be mentioned in Example 6.2.1)
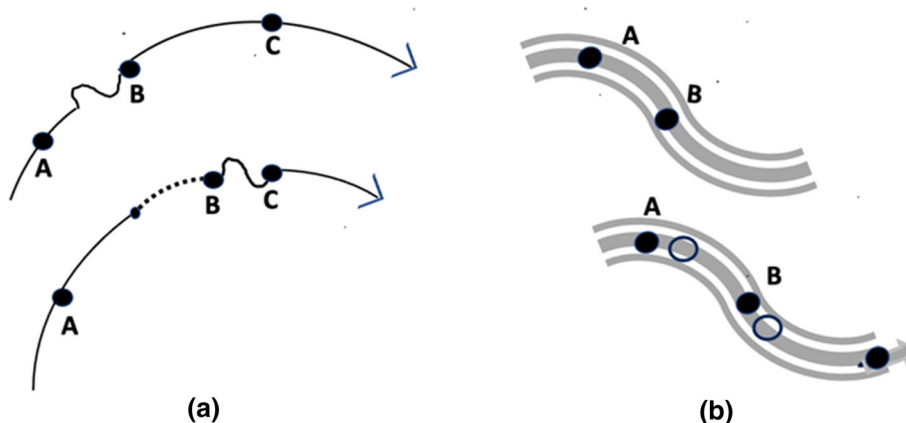

(a)

(b)

Fig. 15 Reptation: A kink in the chain propagates like a soliton; **a** point B on the chain moves and **b** finishes by creeping out of the tube

was called reptation by de Gennes, who described its random motion [51]. He found that instead of the relation $< x^2 > \approx \overline{d^2 \times n} = d^2 \times t/\tau_c$ valid for random walk in 3D (see Sect. 3.1 and previous Example) the restricted motion within such a tube is expected to obey a $< x^2 > \approx t^{1/4}$ behavior.

Fatkullin et al. [52] found excellent agreement with the reptation model in a sample of ethylene-alt-propylene (dPEP, M. 200 k) measured at 450 K. The sample was deuterated and the ^{2}H Hahn-echo amplitude was recorded. Deuteron spin relaxation is caused by its electric quadrupole moment Q interacting with EFG's (electric field gradients) from surrounding molecules (cf. Example 5.1). Various fast processes in the ms range contribute to the initial relaxation, but for times longer than 0.1 s the remaining relaxation is dominated by the reptation process. The time dependence $g(t)$ of the Hahn echo amplitude, which reflects the amount of reptation, was plotted in a log-log diagram to visualize the $t^{1/4}$ dependence at long observation times (Fig. 16).
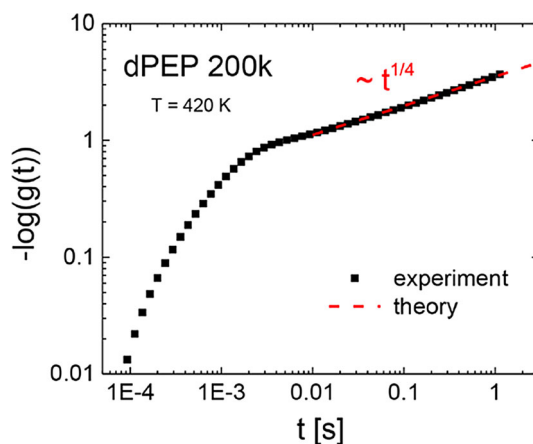
Fig. 16 Negative logarithm of the 2H Hahn-echo amplitude. From [52]

4.1.6 Dynamics in biomolecules

NMR studies of biomolecules accelerated in the 1990's, building on 2D or 3D techniques described in Sect. 2.3.3 and facilitated by the progress in the handling of large quantities of data. An overview of this field is given by Kurt Wüthrich in his Nobel lecture from 2002 [53]. The major advantage of NMR in the study of biomolecules is its access to dynamic information since it can be carried out in with samples in natural liquid environments, unlike X-ray diffraction used for structural analysis which requires crystallized samples. Recent applications are discussed by Alderson and Kay [54].

The different relaxation processes cover a large range of time-scales, from pico-seconds up to minutes. NMR signals are sensitive to the fast processes (ps to ns) involving tumbling and vibration of small molecular constituents and to slower motions (ms—minutes) caused by ligand binding, involvement in catalytic processes or protein folding. Access to the intermediate range (10^{-8}–10^{-4} s) is still a problem, as discussed in a recent article by Ban et al. [55].

At present it is possible, even in large biomolecules like enzymes, to distinguish locally interacting pairs of nuclei in 2D NMR plots obtained by simultaneous r.f.-excitation of (for instance) ^{1}H and ^{15}N isotopes.

One of the most important biomolecules is TIM (triosephosphate isomerase), an enzyme responsible for catalytic processes in most living systems. It is composed of 248 amino acid residues. Figure 17 (reproduced from [56]) is a 2D representation of the chemical shifts of all communicating ^{1}H and ^{15}N nuclei in TIM.

Spin relaxation can be measured selectively in each unit containing a (^{1}H, ^{15}N) pair by addressing the two relevant nuclei at their particular frequencies. In "transverse-relaxation optimized spectroscopy" (TROSY) introduced by Pervushin et al. [57] a special pulse sequence is chosen to minimize local dipole-dipole and chemical shift anisotropies, which leads to a narrowing of the ^{15}N-signals such that a characteristic motion in a specific subunit can be distinguished. Fig. 17c shows relaxation related to a conformation change in the Thr 172 residue in TIM, which is a binding site for an antibody involved (for instance) in the regulation of food intake.

4.1.7 Quantum information processing (QIP)

The possibility to use quantum entanglement as an information resource was considered by Richard Feynman in the 1980's [58] and has since then led to what has been called a "second quantum revolution" [59]. The basic units in quantum information processes are the qubits, two-state quantum systems with wavefunctions $|\psi> = \alpha_0 |0> + \alpha_1 |1> = \frac{1}{\sqrt{2}} (|0> + e^{-\phi}|1>)$. Qubits can be realized in a number of different ways, with the most recent efforts concentrated on superconducting Josephson junctions, but NMR played early (as reviewed by Oliviera in 2012 [60]) an important role in the development of quantum algorithm implementation, quantum communication protocols, simulation of quantum systems, quantum error correction codes and tools to characterize and quantify entanglement.

Sets of nuclear spins with $I = 1/2$ can be used as elements of a quantum computer where the qubits are quantum superpositions of $M_z = +1/2$ and $M_z = -1/2$ states, which represent the $|0>$ and $|1>$ states. A quantum computation requires separate communication with the different qubits (i.e., the different nuclear spins), preparation of qubits (by application of suitable r.f. pulses), and possibility to entangle two different qubits during the computation steps. Quantum coherence must be maintained (or restored if broken) during the whole operation (requiring long T_1-relaxation times for each spin and long spin–spin relaxation times T_2 not to disturb the controlled
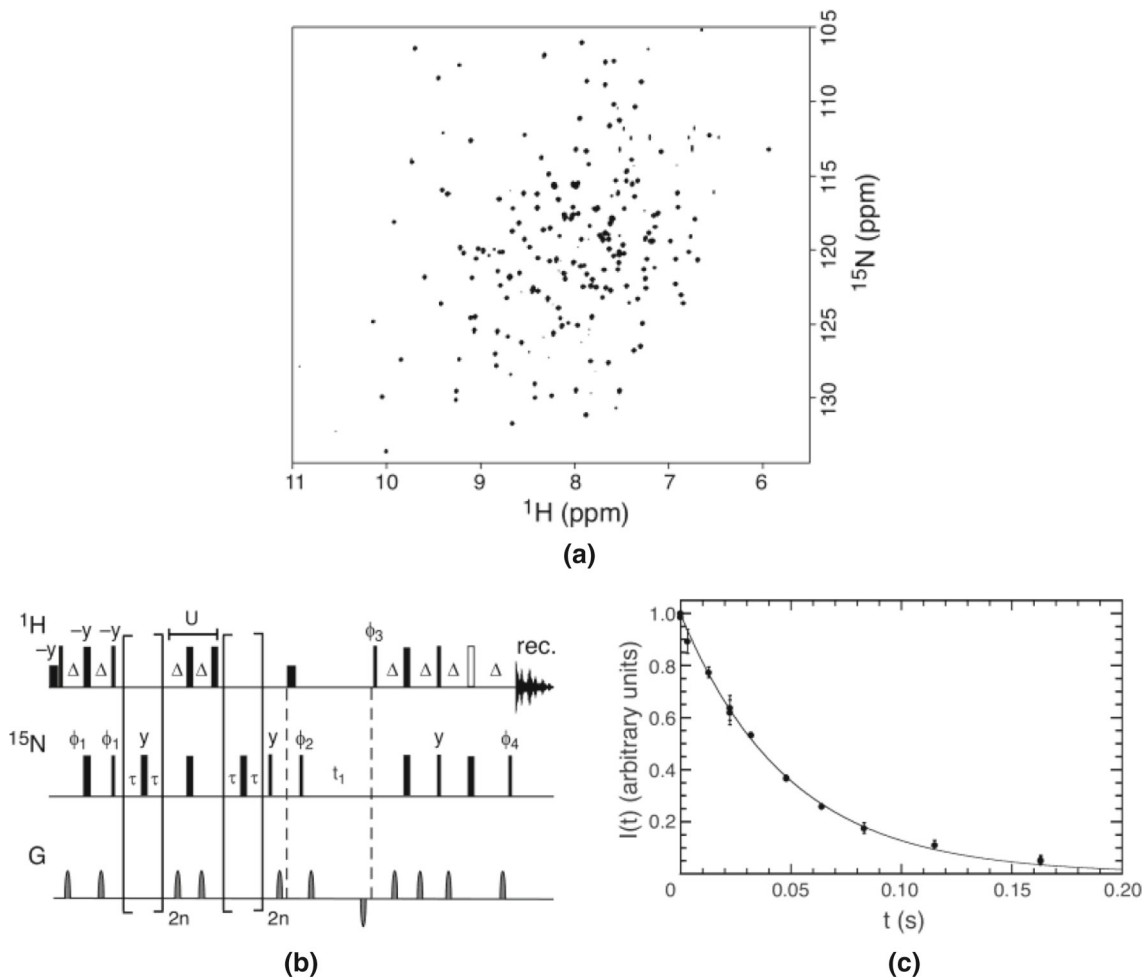
Fig. 17 **a** 2D NMR of TIM (triosephosphate isomerase), **b** pulse sequence used by Loria et al. [58], **c** Relaxation of ^{15}N in the residue Thr 172 with relaxation rate $20.39 \pm 0.36 \ s^{-1}$ [56]

flipping in the entangling process). The long nuclear relaxation times (up to seconds in certain molecules) allow control of the spin systems by complicated pulse sequences.

In a simple application mentioned in Ref. [60], the small molecule chloroform $CHCl_3$ (enriched in ^{13}C), ^{13}C spins play the role of target qubits and ^1H spins the control qubits. They are prepared by pulse sequences turning the separate spins, and are entangled during simultaneous ^{13}C and ^1H irradiation. It is shown how the basic CNOT operation (which performs the NOT operation only when the second qubit is $| 1 >$ and otherwise leaves it unchanged) can be carried out in $CHCl_3$ by application of proper pulse sequences.

Recent progress includes the use of the molecule $FeC_{13}O_2F_5H_2$, where a 3×5 multiplication was carried out with seven qubits, five ^{19}F and two ^{13}C nuclei (Vandersypen et al. [61,62]). However, molecular-based QIP systems have natural limitations in the number of communicating qubits (i.e., pairs of spins with sufficient local interactions) and by cross-talk between neighboring molecules in the samples. Instead, spin-based systems suitable for quantum information are searched in solid environments. One such example will be presented in the section on electron spin resonance (7. 2. 2). As shown in the next example, there are also promising attempts to combine electron and nuclear resonance, as applied to nitrogen vacancy centers in diamond.

In a work by Bradley et al. [63] the electron spin of a single NV center acts as a central qubit and is connected by two-qubit gates to the intrinsic ^{14}N nuclear spin and a further eight ^{13}C nuclear spins surrounding the NV center (Fig. 18). The eight nearest C-nuclei could be separately addressed as shown in the figure. Genuine entanglement between all the 45 possible qubit pairs was confirmed by measuring Bell state fidelities. The problem that the total sequence time in handling such a large number of qubits tended to exceed the natural dephasing time of
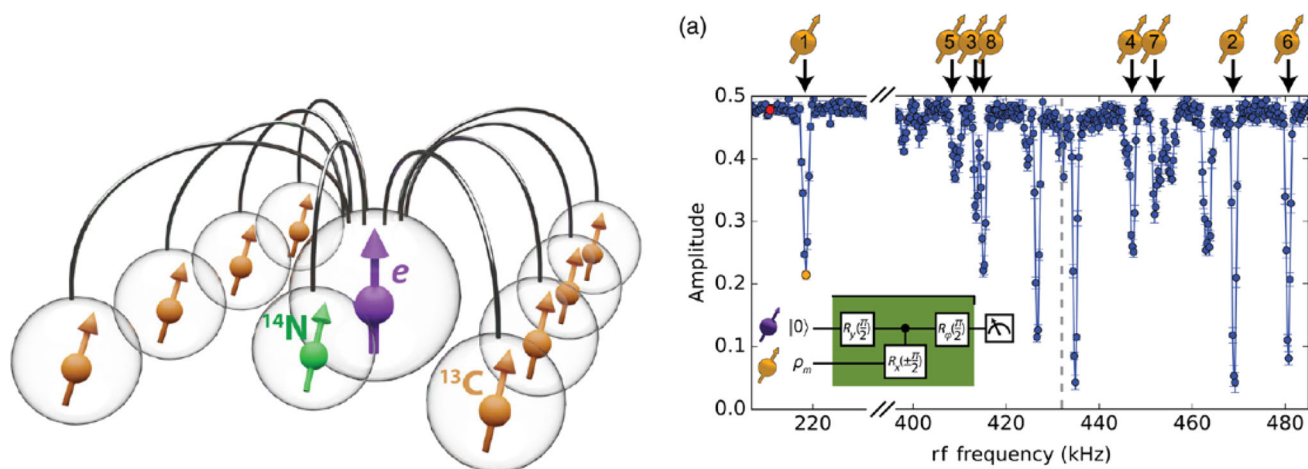
Fig. 18 The electron spin in the NV-center acts as a central qubit and is connected by two-qubit gates to the ^{14}N nuclear spin and a further eight ^{13}C nuclear spins surrounding the NV center. The eight ^{13}C nuclei could be separately addressed. From [63]

the separate nuclei ($T_2 \approx 1$ s) could be remedied by introducing sequences of extra decoupling pulses. Two-qubit entanglement could then be maintained up to 10 s.

5 Internal dynamics, studied by perturbed angular correlations (PAC)

5.1 Short description of the method

Nuclear decays populate excited states of the daughter nucleus, which decay further by emitting γ-rays, often in two steps. The nuclei emitting the first ray γ_1 in a certain direction z_1 have an unequal population of M_I-states with respect to this axis and this partial alignment of the spin substates in the intermediate state I leads to emission of γ_2 with a certain angular correlation $W(\theta)$ with respect to γ_1 (Fig. 19a). Calculations of angular correlation functions for general spin sequences $I_1 \rightarrow I \rightarrow I_2$ were first performed by Hamilton [64]. $W(\theta)$ is measured by detecting coincidences between γ_2 and γ_1. It is expressed in terms of polynomials P_2 and P_4, which are functions of spherical harmonics: $W(\theta) = 1 + A_2 P_2 (\cos\theta) + A_4 P_4 (\cos \theta)$.

If a magnetic field $\mathbf{B}_{\text{ext}}$ is applied along a z-axis perpendicular to the detector plane, the spin I will precess around $\mathbf{B}_{\text{ext}}$ with the Larmor frequency ω_{L}, which leads to a rotation of the γ_2-radiation pattern. This is one form of perturbed angular correlation, PAC. If the lifetime τ_{exc} of the intermediate excited state I is sufficiently long ($\tau_{\text{exc}} > 1/\omega_{\text{L}}$), the spin rotation can be followed in an experiment where γ_1 acts as a start pulse and the decay of γ_2 as the stop. Then an exp($-t/\tau_{\text{exc}}$) decay function modulated by a $\cos(\omega_{\text{L}}t)$ function is recorded by delayed coincidence techniques; this is time-differential PAC, or DPAC. Figure 19b shows the modulation with the exponential decay subtracted (from Matthias et al. [65]).

Normalized DPAC-curves are analogues of the FID's in NMR. They show damping through interactions with internal magnetic dipolar fields or fluctuating electric field gradients. The sensitivity is high because of the strong initial alignment of the nuclear spin system and high detection efficiency for gamma ray photons, but the DPAC method is limited by the scarcity of nuclear excited states with sufficiently long τ_{exc}. Advantages are that internal magnetic fields in ordered magnets can be studied without applying external magnetic fields and that signals can be detected even from extremely dilute radioactive impurity atoms in solids. A review by Karlsson [66] from 1995 covers applications of PAC to problems in magnetic and semiconducting materials, as well as studies of defects in solids and on surfaces.

5.2 Examples

5.2.1 Spin fluctuations and viscosity in liquids

PAC is of the same age as NMR. Determination of magnetic moments of excited nuclear states by PAC were proposed by Goertzel in 1946 [67] and the first experiments were published by Aeppli et al. in 1951 [68]. They measured the magnetic moment, $\mu = -0.85(22)\ \mu_N$, of the first excited state in ^{111}Cd (at 247 keV, $\tau_{\text{exc}} = 133$ ns), by observing the effect on the angular correlation pattern in a magnetic field of 0.42 T. These early experiments could not
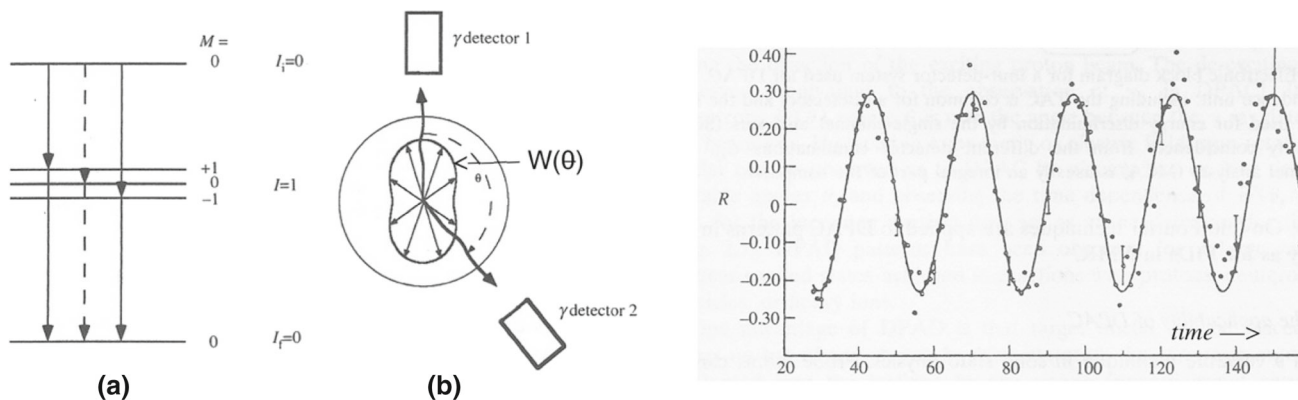
Fig. 19 Left panel: **a** simple example of gamma–gamma decay, providing unequal population of I_M-states (spin alignment); **b** turning of $W(\theta)$ in perpendicular field. Right panel: Spin-rotation pattern from a gamma-gamma cascade in ^{100}Rh in a magnetic field of 0.2 T [65]
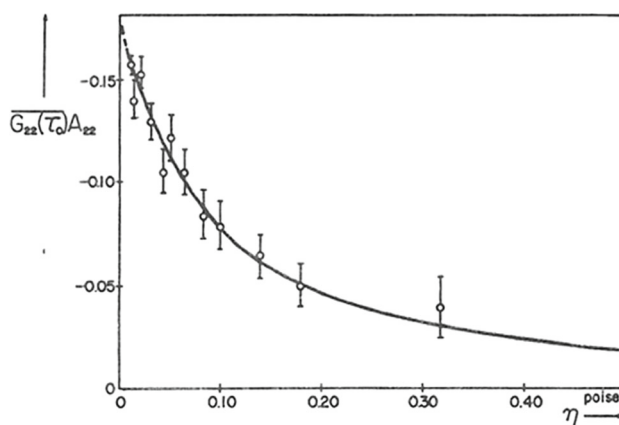

Fig. 20 The $\gamma - \gamma$ correlation factor $G_2(\tau_c)A_2$ measured for solutions of different viscosities [69]. The true value of A_2 is found to be -0.18

resolve nano-second events and measured the time-integrated effect, $W(\theta, \infty) = \int \exp(-t/\tau_{\rm exc}) \, W(\theta, t){\rm d}t$, only. Nuclear relaxation was a source of error in measuring the angular correlation $W(\theta)$ as well as the magnetic moments when relaxation rates were of the order of $1/T_1 \approx \tau_{\rm exc}$. It prompted separate investigations, in the absence of $B_{\rm ext}$, of perturbation factors G_2 and G_4 multiplying $A_2P_2(\cos \theta)$ and $A_4P_4(\cos \theta)$ in the expression for $W(\theta)$.

Hemmig and Steffen [69] measured the time-integrated factor $G_2(\infty)A_2$ in the ^{111}Cd angular correlation with the radioactive radioisotope ^{111}In dissolved in liquids of different viscosities (Fig. 20) (cf. Example 4.1.1). For fast fluctuations, relaxation is exponential with λ_2 proportional to $\sigma_{\rm int}^2 \tau_c$,

$$G_2(\infty) = (1/\tau_{\rm exc}) \int_0^\infty \exp(-\lambda_2 \, t)\exp(-t/\tau_{\rm exc}){\rm d}t = 1/(1 + \lambda_2/\tau_{\rm exc}) \qquad (7)$$

Abragam and Pound [70] provided theoretical expressions for $\sigma_{\rm int}^2$ for magnetic and electric interactions. For the actual nuclear state, which has spin $I = 5/2$ and a large nuclear quadrupole moment Q, the electric interaction with local field gradients Vzz is dominant and λ_2 is related to the fluctuation rate τ_c by $\lambda_2 = (3/80)(eQ/\hbar)^2 \, Vzz^2[6 \times (4I(I+1)-4)/I^2(2I-1)^2] \times \tau_c$.

The data follow Eq. (7) as expected if τ_c is proportional to the viscosity η. Extrapolation to zero gives the true value of A_2. Relaxation was a severe problem for nuclear physicists when deriving magnetic moments and multipole character of the gamma rays involved from the radiation patterns.

5.2.2 Critical spin fluctuations in magnets (Ni)

A few DPAC isotopes allow a detailed recording of spin precession curves. One of them is ^{100}Rh which has an excited state at 74 keV with lifetime 3.39×10^{-7} s. It was used by Hohenemser et al. [71,72] to study critical phenomena. When doped in as an impurity atom in ferromagnetic Ni it feels a local field $B_{\rm loc}(0) = 22.5$ T at
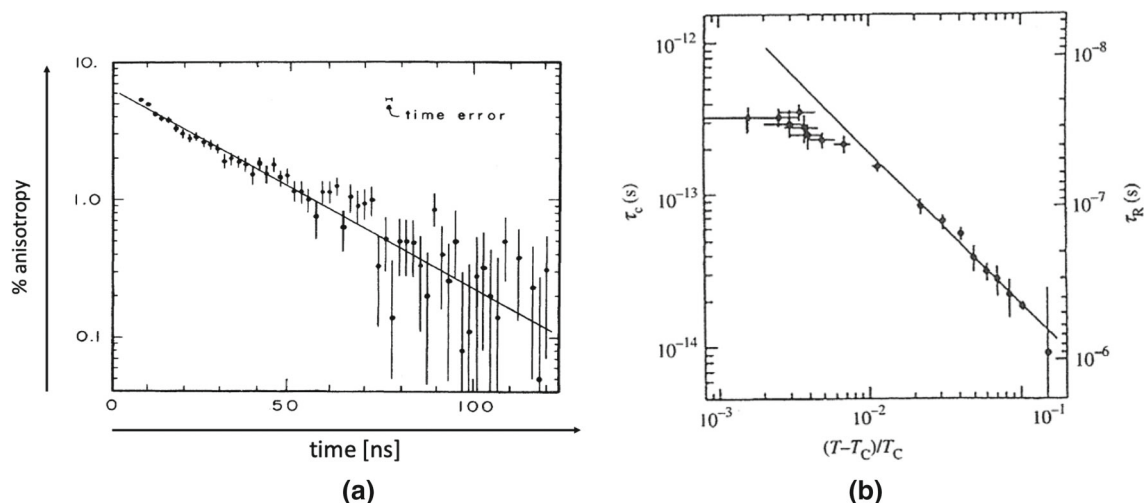
Fig. 21 **a** Decay of spin alignment (T_1 relaxation), **b** determination of the critical exponent n from DPAC experiments, both from [72]

low T, produced by the surrounding ordered Ni moments. In the critical range near T_C (Curie temperature) the magnetic ordering $< M >$ just below Tc and the magnetic fluctuations τ_S just above T_C are expected to follow scaling laws, i.e., exponential dependencies on the ratio $\varepsilon = (T - T_C)/T_C$.

$$< M(T) > / < M(0) >= [(T_C - T)/T_C]^{\beta}; \quad \tau_S = [(T - T_C)/T_C]^n. \tag{8}$$

Suter and Hohenemser [71] first measured $\beta = 0.382(3)$ within the range $10^{-2} > \varepsilon > 10^{-4}$, a value close to the theoretical expectation, $\beta = -3/8 = -0.375$, by observing spin rotation in the internal field. Soon after, Gottlieb and Hohenemser [72] measured n within the range $10^{-2} < \varepsilon < 10^{-1}$. In both types of measurements PAC had the advantage that no external magnetic field is needed, by which so-called rounding corrections are avoided.

For $T > T_C$ there is no static magnetic field acting on the nuclei but their spin alignment is smeared out when the electronic spins relax. Figure 21a is a recording of the time decay of the angular correlation anisotropy at the reduced temperature $\varepsilon = 5.9 \times 10^{-4}$, showing an exponential decay $\exp(-\lambda_2 t)$ with $\lambda_2 = \sigma_{\text{int}}^2 \tau_S$ and Fig. 21b the variation of τ_S for different ε. Knowing $B_{\text{loc}}(0)$ from low-T measurements, σ_{int}^2 could be calculated and the electronic spin fluctuation times τ_S calculated. Because of the high σ_{int}^2 it was possible to follow τ_S down to the 10^{-14} s range. The slope in Fig. 21b corresponds to $\tau_S = [(T - T_C)/T_C]^n$ with $n = -0.70(3)$, which was compared to what could be expected from scaling theory for dynamical critical exponents.

6 Muon spin rotation (or relaxation), MuSR

6.1 Short description of the method

The positive muon μ^+ is an elementary particle with spin $I = 1/2$ and a mass about one tenth of the proton, $m_\mu = 0.11\, m_p$. It is produced in the decay of the positive pion $\pi^+ \rightarrow \mu^+ + \nu_\mu$, where ν_μ is a muon neutrino, and the μ^+ decays with a lifetime $\tau_\mu = 2.2 \times 10^{-6}$ s into a positron, an electron neutrino and a muon antineutrino: $\mu^+ \rightarrow e^+ + \nu_e + \bar{\nu}_\mu$. For the production of the pions, an accelerator with $E_p > 200$ Mev is necessary; MuSR-experiments are therefore performed only in a few laboratories (at present five or six) in the world.

The muon and the pion decays are both weak interaction processes, which means that specific symmetry relations apply: neutrino spins $\mathbf{s}_\nu$ must be in the opposite direction to their momenta $\mathbf{p}_\nu$. If the pion (whose spin is zero) decays at rest the muon created must also have its spin $\mathbf{s}_\mu$ opposite to its propagation direction. In the subsequent muon decay, angular momentum is shared by the positron e^+ and the two neutrinos, but by selecting only high energy e^+ decays the positron angular distribution $W_{e+}(\theta)$ is still strongly peaked, see Fig. 22a. Since $g_\mu = -2.0023$, the magnetic moment $< \mu_\mu >$ lies along $< \mathbf{p}_{e+} >$.

Positive muons are implanted into the materials to be investigated. In crystals they take up interstitial positions in the crystal lattice, in organic molecules they replace one of the protons because they are chemically different from protons only with respect to their mass. They start their spin precession or relaxation with a definite orientation, $P(+S_\mu) > P(-S_\mu)$ (i.e., not only with an alignment, where $P(-M_I) = P(+M_I)$, as in PAC). The spin orientation
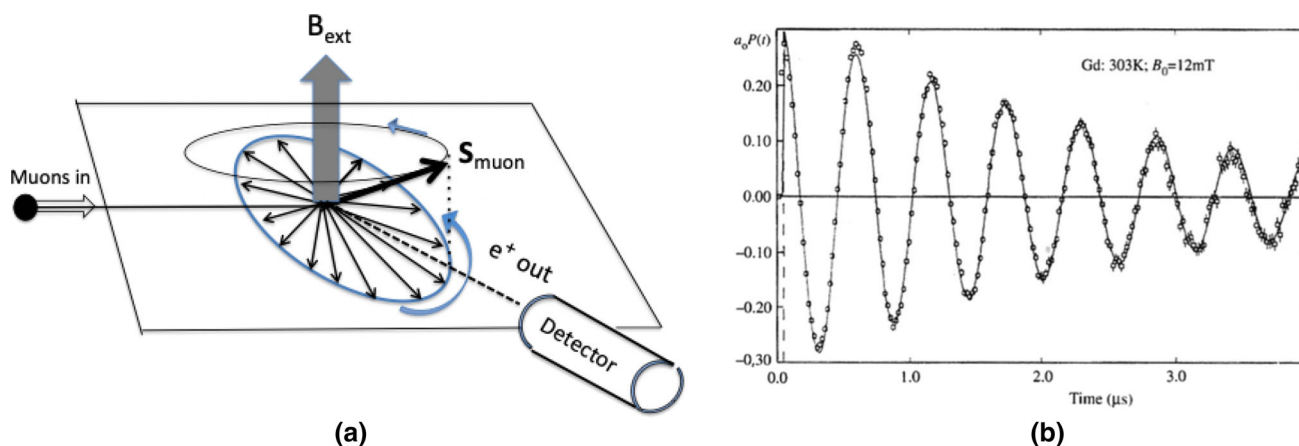
Fig. 22 **a** Principle of MuSR **b** spin rotation of μ^+ implanted in Gd, measured above T_C

relative to sample axes can be chosen by the experimenter and is used to advantage in certain experiments, see below. Figure 22b is a typical example of a damped spin precession at $B_{\text{ext}} = 12$ mT, recorded by MuSR.

MuSR has been described in textbooks by Schenck [73], Karlsson [66] and, recently by Yaouanc and Dalmas de Réotier [74]. The positive muon is used as an internal magnetic probe, but also as a substitute for hydrogen in experiments exploring the diffusion of light elements in solids [75]. In metals, its positive charge is screened by itinerant electrons within a short distance, but in semiconductors and insulators it picks up a bound electron, forming muonium, Mu. Muonium spectroscopy involves the strong a $\mathbf{I}_\mu \cdot \mathbf{S}_e$ coupling with precession frequencies in the 100 MHz range and resembles ESR, but is not illustrated here.

6.2 Examples

6.2.1 Trapping of mobile positive muons in metals

In Sect. 3.1, Fig. 7 shows a crystal lattice with an atom placed in an interstitial site. These sites are the preferred stable positions for the lightest elements (H, He, Li) when present in heavier crystals. As mentioned in the Example 4.1.4, they are mobile and diffuse easily even at relatively low temperatures. This is expected to be more pronounced for the positive muon, μ^+, which acts like a proton with reduced mass, $m_\mu = 0.11\, m_{\text{p}}$. In an experiment with μ^+ in niobium hydride NbH$_{0.86}$ by Karlsson et al. [76], the T-dependence of the diffusion coefficient D_H in Example 4.1.4 (Fig. 14b) was reproduced perfectly, with activation energy almost equal for the proton and the muon and $D_\mu = (1/6)\, d^2/\tau_c \approx D_H$. This could be explained by the fact that the muon in an ordered hydride could move only when a proton leaves its position.

Metals used for construction or as reservoirs for hydrogen usually contain hydrogen and other impurities (N, C and heavier elements) at the 10–100 ppm level. When hydrogen is present as an impurity it may cause severe problems (hydrogen embrittlement) if it reaches grain boundaries. An intermediate step is the process of trap-limited diffusion (which for hydrogen in metals may take days, and for carbon in steel perhaps many decades at ambient temperatures). If the positive muon is used to simulate hydrogen motion it can—due to its very much higher intrinsic mobility—in a very short time give detailed information on this process.

In such experiments, the positive muons are implanted one by one at random in a metallic lattice. Like the protons, they sooner or later find a lower potential well near an impurity atom (Fig. 23a). At intermediate temperature, it may remain there for a long time compared with the muon lifetime τ_μ, $(\tau_{\text{trap}} > \tau_\mu)$, but when the temperature is raised it may leave the trap during the observation time range and diffuse freely again. Hartmann et al. [77] studied the trap-limited diffusion for μ^+ in Al-metal doped with known amounts of different impurities. The observed dependence on temperature (Fig. 23b) could be understood as a two-step process, each involving a motional narrowing like that shown in Example 4.1.4. It was analyzed in terms of coupled Arrhenius equations for trapping and release. Arrhenius parameters for motion in the pure Al-lattice as well from the traps could be determined. It could also be inferred by the help of Eq. (3) that muons in the pure Al-lattice occupy positions of octahedral symmetry, but those trapped close to an Mn-impurity in Al are found at a tetrahedral site [78] (cf. Fig. 7).

The fast diffusional motion of muons in metals was called "quantum diffusion." It could be described by an Arrhenius relation (whose activation energy E_μ turned about to be about half of that of the proton E_{p}), but with a very low prefactor, $\nu_\mu \approx 10^{-5}\nu_{\text{p}}$, which indicated that muons do not jump over barriers, but tunnel through them. However, the process is still a diffusion in the sense that quantum coherence is lost between each step. Karlsson et al. [78] asked the question whether decoherence could be reduced to such an extent that quantum
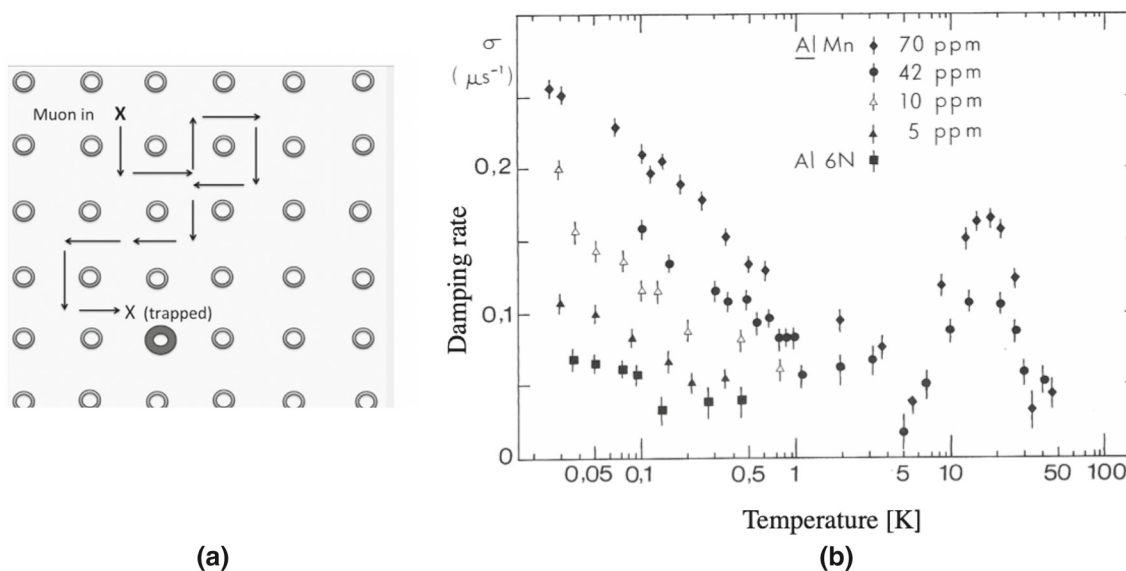
Fig. 23 **a** Trapping of a muon at an impurity, **b** Damping rates of muon precession in Al doped with different amounts of Mn [77]

coherence is maintained over several tunneling steps (which would correspond to a "propagation," like that of electrons in a metal). The test material was again very pure Al-metal, now doped with 8, 18 and 75 ppm Li-atoms and the experiments were performed below $T_{sc} = 1.1$ K where Al is superconducting. Below T_{sc}, trapping in the superconducting state could be compared with that in the normal state (achieved by quenching superconductivity in a weak magnetic field). Its rate was very much higher and indicated a transition from quantum diffusion to propagation when the sample becomes superconducting. The explanation was that decoherence caused by interaction with conduction electrons is then strongly reduced because of the energy gap. In the purest sample, muons were never trapped during the observation time (10 μs).

6.2.2 Spin fluctuations in paramagnetic gadolinium

Gadolinium is a ferromagnet below $T_C = 294$ K. In contrast to nickel, discussed in Example 5.2.2, its magnetism results from the ordering of local f-electrons residing of each of the Gd atoms, whose ground state is of $^8S_{7/2}$ character. Positive muons have been implanted in Gd to study the details of spin dynamics from T_C up to the high-T limit. The local contact field B_{loc} at the muon sites is dominated by the dipolar field B_{dip} produced by the nearest Gd moments and spin precession curves are damped by an exponential factor $\lambda = \gamma_\mu^2 B_{loc}^2 \tau_S \approx 7 \times 10^5 \times \tau_S$ in the fast fluctuation limit.

In the paramagnetic range spins are still correlated, but with short-range order. There are clusters of partially ordered spins with correlation lengths ζ, which vary from several nanometers close to T_C down to the Gd–Gd distance limit ($d = 0.36$ nm) at high-T. MuSR techniques made it possible to follow the variation of τ_S from $\varepsilon = (T-T_C)/T_C = 0.002$ up to $\varepsilon = 2$, i.e., 600 K. In the high-T limit with near-neighbor spins interacting only, τ_S is expected to be equal to $\tau_{exch} \approx \hbar/J_{exch} \approx 10^{-13}$ s, where J_{exch} is the exchange integral.

The results of experiments by Hartmann et al. [79] are shown in Fig. 24a. In a logarithmic plot of λ versus $(T-T_C)$, the fluctuation rate could be described by a single critical exponent ε^n when measured with an external field (squares in plot). On the other hand, in zero-field relaxation experiments, data in the range T_C to $(T_C + 12)$ K deviated strongly; the critical exponent was "broken" (circles in Fig. 22a). The explanation was that local spin–spin interaction in Gd is not only a quantum exchange effect (as in Ni),_but also_a dipolar coupling effect:

Dipolar coupling is <u>not spin-conserving</u>. In the expression for the dipolar interaction,

$$H_{dip} \approx a_{dip}\{[\mathbf{S}_i \bullet \mathbf{S}_j - 3(\mathbf{S}_i \bullet \mathbb{r}_{ij})(\mathbf{S}_j \bullet \mathbb{r}_{ij})]/r_{ij}^3)\} \tag{9}$$

the first term $\mathbf{S}_i \cdot \mathbf{S}_j$ commutes with $J_{exc} \mathbf{S}_i \cdot \mathbf{S}_j$ for the exchange coupling, but the second term only if the spin ordering is perpendicular (transverse) to the position vector $\mathbf{r}_{ij}$ between the two spins. If it is parallel to it, all longitudinal spin waves within the clusters are destroyed when their energy $E = Dq^2$ is less than the dipolar interaction energy E_{dip}. But the spin wave momentum q is limited by the size of the cluster with maximum $q_d \approx 2\pi/\zeta$, so that a break point is expected at a correlation length $\zeta \propto \sqrt{(D/E_{dip})}$. Numerical data on D and E_{dip} predict a break point at $\zeta = 1.2$ nm, which [knowing $\zeta(\varepsilon)$ from neutron data [80]] corresponds to a temperature
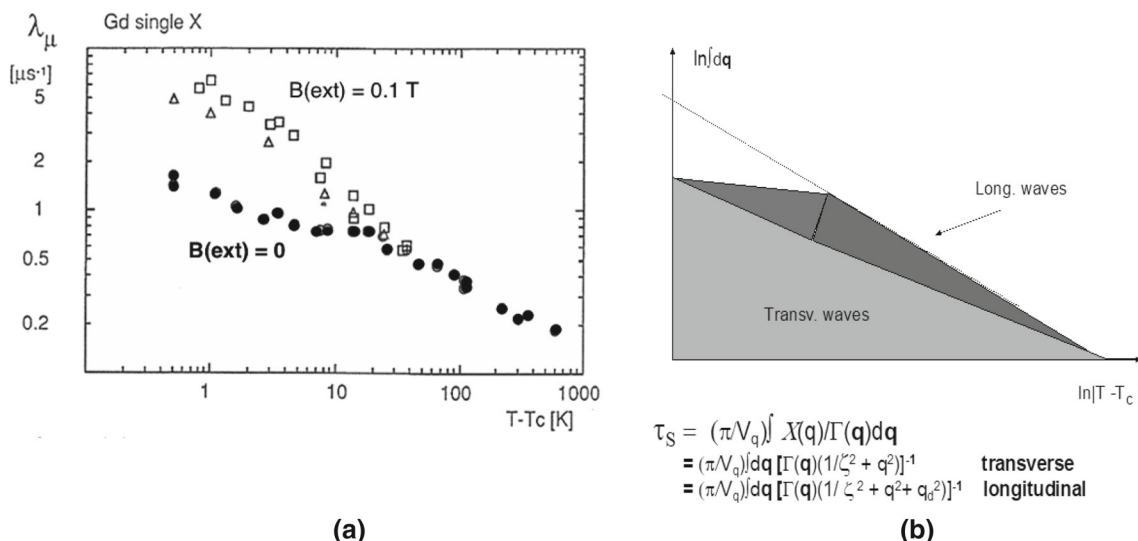
Fig. 24 **a** Damping rates λ_μ (proportional to τ_S) above T_C in Gd (circles in $B_{ext} = 0$, squares in $B_{ext} = 0.1$ T), from [79], **b** contributions to damping in $B_{ext} = 0$ from trans-

verse and longitudinal spin waves in Gd-clusters. X(q) and Γ(q) are neutron scattering functions, each having a critical exponent
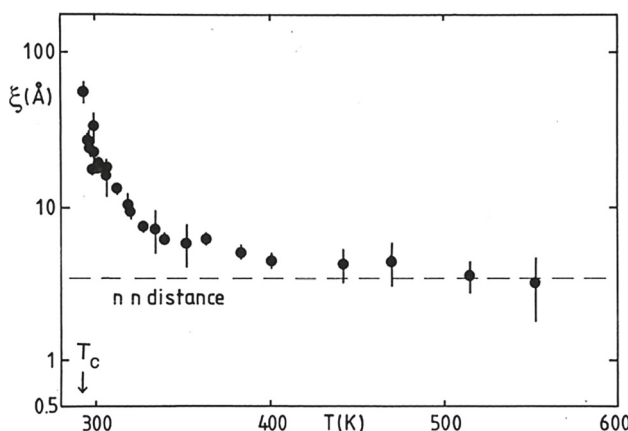

Fig. 25 Spin correlation lengths in paramagnetic Gd extracted from correlation times [81]

near the break point observed, $T_C + 10$ K. In external fields with $g_s\mu_B\mathbf{S} \cdot \mathbf{B}_{ext} >> E_{dip}$, the longitudinal spin waves are restored. The critical exponent was found to be $n = -0.45(8)$, indicating mean field theory behavior.

Small magnetic clusters still remain up to high temperatures ($T \approx 2T_C$). An approximate relation between correlation lengths ζ and spin correlation times τ_S is obtained [81] by considering the spatial part of the spin auto-correlation function, $G_s(i,j) = G_0(\tau_S)\exp[-r_{ij}/\zeta(T)]$. Considering two spin states ($|M_S >=$ up) and ($|M_{S-1} >=$ down), the probability for a flip of spin i (assumed "up") is proportional to the probability for spin j to be "down" since the Heisenberg mechanism only works by flips of pairs of opposite spins. Since $G_s(\tau_S) = 1$ without flip, the flip rate is proportional to $1 - G_s(\tau_S)$, from which follows that $\tau_S(T) = \tau_{exch} [1 - exp(r_{ij}/\zeta(T))]^{-1}$. With $r_{ij} = 3.6$ Å and correction for the so-called Korringa relaxation (by conduction electrons), the τ_S data were transformed to $\zeta(T)$ data after normalization at 320 K where $\zeta = 10$ Å [80] as shown in Fig. 25. The correlation lengths approach the Gd–Gd-distance for $T = 2T_C$, with $\tau_{exc} \approx 3 \times 10^{-13}$ s.

6.2.3 Critical fluctuations in a strongly anisotropic magnet

Metallic Erbium is an antiferromagnet with a Néel temperature of $T_N = 85$ K. In the range 52–85 K, it is strongly anisotropic with moments aligned along the hexagonal c-axis. Wäppling et. al. [82] used the unique possibility to start the precession with an initial preferred direction of the muon spins in an investigation of the critical behavior near T_N in a single crystal of Er (Fig. 26a). The MuSR signal was damped by fluctuations in the local field B_{loc}
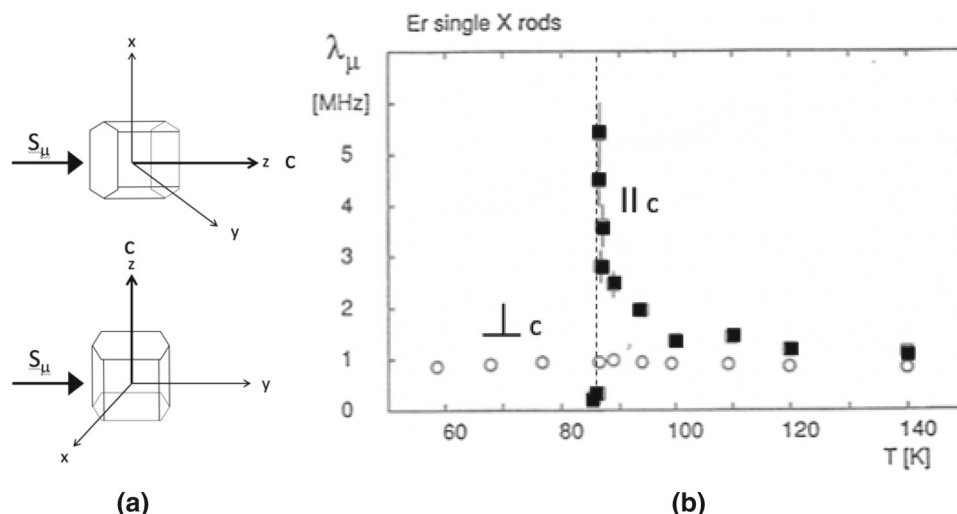
Fig. 26 **a** Implantation with muon spin parallel and perpendicular to crystalline *c*-axis **b** critical slowing down (λ is proportional to τ_s) of spin component parallel to *c* (squares), but not for spins perpendicular to *c* (circles). From [82]

at the muon sites, with factors

$$\lambda_{||c} = \gamma_\mu^2 \int \mathrm{d}\tau [< B_{\mathrm{loc},\perp}(\tau) B_{\mathrm{loc},\perp}(0) > + < B_{\mathrm{loc},\perp}(\tau) B_{\mathrm{loc},\perp}(0) >] \tag{10a}$$

$$\lambda_{\perp c} = \gamma_\mu^2 \int \mathrm{d}\tau [< B_{\mathrm{loc},||}(\tau) B_{\mathrm{loc},||}(0) > + < B_{\mathrm{loc},\perp}(\tau) B_{\mathrm{loc},\perp}(0) >] \tag{10b}$$

for $\mathbf{S}_\mu$ along the *c*-axis and perpendicular to the *c*-axis, respectively. From the two data sets measured, the correlation functions $< B_{\mathrm{loc},||}(\tau) B_{\mathrm{loc},||}(0) >$ and $< B_{\mathrm{loc},\perp}(\tau) B_{\mathrm{loc},\perp}(0) >]$ could be obtained separately and their T-dependences are displayed in Fig. 26b.

The experiment demonstrated clearly that only the $B_{\mathrm{loc},||}$ fields (and therefore the $M_{||}$ magnetization) goes critical when T_N is approached from above, while $B_{\mathrm{loc},\perp}(M_\perp)$ fluctuations are unaffected over the passage of T_N.

6.2.4 Critical fluctuations in a 2D-magnet

A final example of critical fluctuations will be mentioned briefly. Scaling laws predict different critical exponents for ordering in 2D and 3D-systems. Lidström et al. [83] tested the validity of scaling laws in a MuSR experiment on the quasi-2D antiferromagnets REGa$_6$ (Fig. 27) where the Rare Earth (Ce, Nd, Gd, Tb) layers are separated by about 10 Å. The implanted muons came to rest in the Rare Earth layers and experienced local fields of the order of 1 T. The example chosen here is NdGa$_6$, which has a Néel temperature $T_\mathrm{N} = 10.4$ K.

It is noted that magnetic clusters remain up to $T \approx 10\ T_\mathrm{N}$ and that $\lambda = \gamma_\mu^2 B_{\mathrm{loc}}^2 \tau_\mathrm{S}$ decreases more slowly as function of the reduced temperature $\varepsilon = (T - T_\mathrm{N})/T_\mathrm{N}$, as compared to the 3D magnet Ni (Example 5.2.2). The τ_S data follow an ε^n law with $n = -0.61(5)$, which can be compared with dynamical scaling predictions for n: The n exponent is supposed to be related to the exponent for the correlation length ν and the one for the $\Gamma(q)$ parameter in the neutron scattering function $S(q,\omega)$ (= 2 in 2D) by the scaling relation $n = \nu(z + 2 - d)$, where d is the dimensionality. With $\nu = 0.7$ (known from the neutron experiments), the theoretically expected value for the correlation time would be $n = -0.7$.

7 Electron spin resonance (ESR) or electron paramagnetic resonance (EPR)

7.1 Short description of the method

The energy splitting between the electronic $M_\mathrm{S} = +1/2$ and $-1/2$ sublevels in standard EPR experiments corresponds to frequencies in the GHz range, which requires wave-guide arrangements. An X-band spectrometer operates at about 3 cm wavelength with a frequency about 9.5 GHz, which requires a magnetic field of about 0.34 T and *Q*-band spectrometer with 35 GHz a field of 1.25 T. Recent developments have increased the frequency range to 1–200 GHz. Resonances are detected by microwave absorption intensity $\alpha(B_{\mathrm{ext}})$.
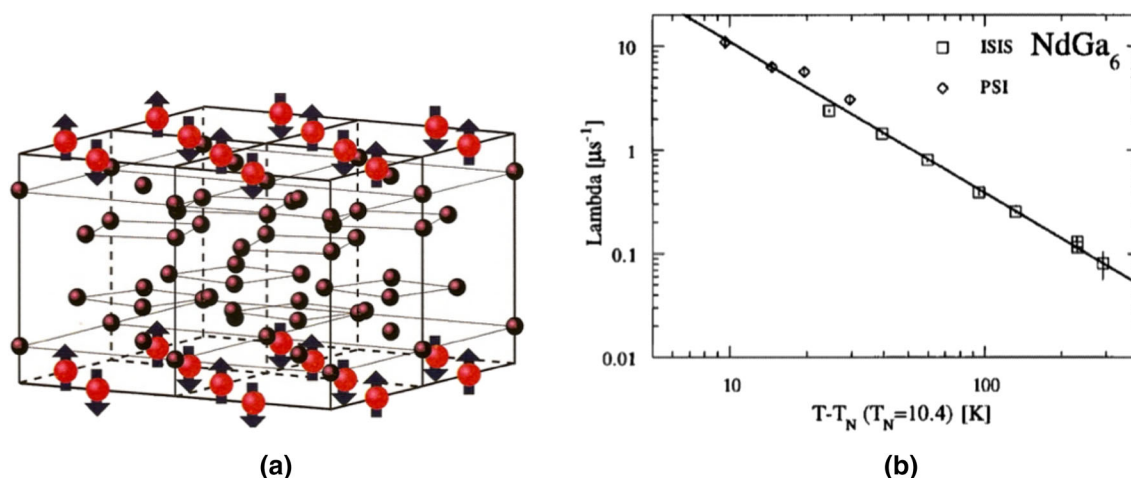
Fig. 27 **a** Quasi-2D-layered NdGa$_6$-crystal with antiferromagnetic Nd-atoms (red arrows), **b** Spin relaxation rates (λ is proportional to τ_s) above T_N. From [83]

In standard instruments the magnetic field is swept through the resonance and the derivative of the microwave absorption $d\alpha/dB_{\text{ext}}$ is recorded. If the electron interacts with a nearby nucleus of spin $\mathbf{I}$, resonances are is split by the hyperfine interaction $a\,\mathbf{S}\cdot\mathbf{I}$. Splittings are used to characterize paramagnetic spin environments, for instance in polymers and biomolecules. More detailed information on local structure around paramagnetic centers can be obtained by combinations of NMR and EPR (ENDOR, introduced by Feher in 1956 [84]).

Free electrons interact strongly with their environment. Spin relaxation times are typically 10,000 times shorter than in NMR, between 0.1 and 10 μs for T_1 and somewhat shorter for T_2. In early EPR experiments, very short pulse techniques were not available and relaxation could not be followed directly on the time-scale, like in NMR. It could be derived from measured linewidths (or from observation of recovery after saturation of signals) only and dynamic information from EPR was limited. Another limitation was the large inhomogeneous broadening caused by imperfections in growth of crystalline samples.

Over the last 30 years, technology has progressed and spin echo techniques with 10–100 ns pulses can now be applied in EPR, as described in the text-book by Schweiger and Jeschke from 2001 [85]. These methods give primarily structural information, concerning environments of metallic centers in proteins, hydration of biomolecules, etc., but information on molecular dynamics can also be deduced from EPR-spectra. They have also been applied extensively in studies of photosynthesis [86].

Many activities in EPR are related to observation of free radicals. They may be present in materials where they have been formed by excessive heating or by ionizing radiation, but in some experiments molecules with relatively stable radicals, like trityl (tetrathiatriarylmethyl) are also added as labels, in order to observe signals from regions to which they are bound.

7.2 Examples

7.2.1 EPR imaging of living tissue

EPR-imaging was introduced in the 1990's, as described by Halpern et al. [87] and Eaton and Eaton [88]. It works with signals in the ms range and can be performed with a spatial resolution of 1 mm^2. Figure 28 (from [88]) is an example of oximetry (determination of in vivo concentration of O$_2$) in a mouse tumor, doped with trityl radicals. The shortening of the spin relaxation times when oxygen molecules collide with the trityl is a measure of the oxygen concentration. Oximetry is crucial for the diagnosis and monitoring of tumors, wound healing and cardiac function.

7.2.2 Preservation of coherence in a solid-state spin qubit

Unpaired electron spins are also found in insulators containing vacancies. This has attracted the interest of quantum information scientists since it offers possibilities to use electronic spins states as bases (qubits) for computer elements. In Example 4.1.7 nuclear spins were used for the same purpose; they showed long relaxation times allowing complicated quantum operations, but the number of possible qubits was limited. Vacancy states in silicon or diamond are promising candidates for multi-qubit devices based on electron spins and can be addressed by optical resonance as well as microwave signals.
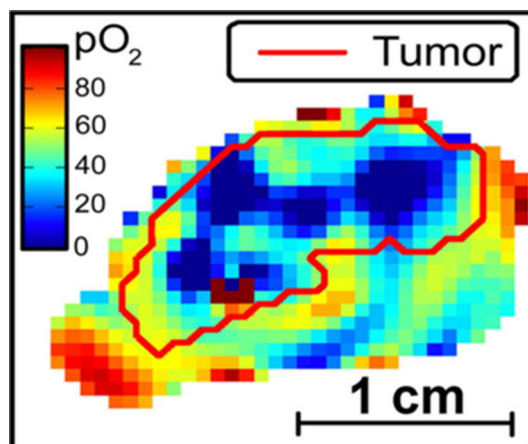
Fig. 28 Oxygen concentration obtained from spin-echo images of the trityl radical OX063 injected into a mouse intravenously. Images were obtained at 5 different echo times from 0.7 to 2.4 μs to obtain T_2 relaxation rates in each voxel [88]. The contour was simultaneously recorded by MRI
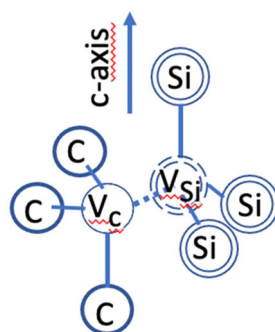

Fig. 29 The di-vacancy in SiC

The short spin relaxation times for electrons in solids, with T_2 of the order of μs, is a main limitation for coherent operations, but in a recent paper, Miao et al. [89] showed how T_2 relaxation can be prolongated by a factor 1000 for the two electron spins in the so-called kh divacancy in 4H–SiC (Fig. 29). The motion of the total spin $\mathbf{S} = 1$ of the two unpaired electrons is governed by the Hamiltonian $H = DS_z^2 + E(S_x^2 - S_y^2) + \gamma_e \mathbf{B}_{\text{ext}} \cdot \mathbf{S}$, where D is the longitudinal field splitting and E the transverse zero-field splitting, which arise from quasi-static nuclear moments in the host material.

The stabilization of the electron spin motion by the external field was already a large improvement, but another factor of 100 in decoherence protection could be obtained by driving a microwave field with Rabi frequency Ω, which added a $\Omega \cos(\omega t)$S term to the Hamiltonian. It produced a dressed photon-electron state, in whose bases the persistence of the qubit $(1/\sqrt{2})[|+1> +|-1>]$ was measured. In this decoherence protected subspace (DPS), T_2 was extended to 22 ms.

8 Ferromagnetic resonance (FMR)

8.1 Short description of method

Ferromagnetic resonance was first observed by Griffiths in 1946 [90] and interpreted in detail by Kittel in 1948 [91]. Like EPR it works with microwaves, which are enclosed in a cavity placed in an electromagnet, whose field B_{ext} is varied to find the resonances. It is applied to magnetic materials, where the partially ordered electrons respond to the microwaves. It is a standard tool for studying spin waves and spin dynamics, now applied extensively to magnetic thin films.

In the natural state the field experienced by the electrons is the internal field B_{int} (of the order of 100 T) from the surrounding magnetic moments, which are directed along the easy magnetization direction and produce a bulk magnetization density $\mathbf{M}$. Application of an external field $\mathbf{B}_{\text{ext}}$ along the easy axis (which requires single crystal samples) shifts the magnetic energy by $\pm\hbar\gamma_e\mathbf{B}_{\text{eff}}$ and turns the spins by the Larmor frequency $\omega_L = \gamma_e\mathbf{B}_{\text{eff}}$. Here,
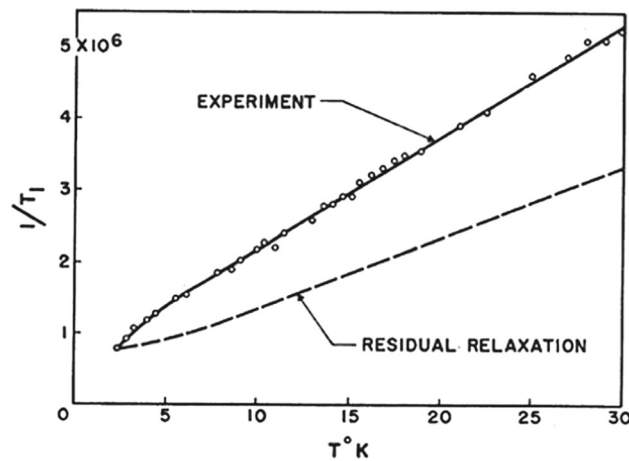
Fig. 30 Electron spin relaxation rate as function of temperature in YIG [92]

$\mathbf{B}_{\text{eff}}$ is different from $\mathbf{B}_{\text{ext}}$ because of demagnetization effects: $B_{\text{eff}} = \mathbf{B}_{\text{ext}} - N\mathbf{M}$, with N determined by the shape of the sample.

8.2 Examples

8.2.1 T_1-relation to spin wave temperature

The work by Spencer and LeCraw [92] provides an early example of spin relaxation in a magnetic material. They studied a sphere of yttrium iron garnet (YIG) at low temperature. The T_1 relaxation time was found to be 1.5×10^{-6} s at 2.5 K with a linear dependence on temperature (Fig. 30). After correction for effects of paramagnetic rare earth impurities, there remained a residual relaxation, still with a linear T-dependence, $(1/T_1) \approx 10^5 T \text{s}^{-1}$.

The residual relaxation was interpreted by Sparks and Kittel [93] as a result of spin wave "S-modes" coupling to the thermal vibrations through Raman scattering, which involves a magnetic dipole interaction. Based on these assumptions they derived a theoretical relation between $(1/T_1)$ and the spin-temperature T_{sp} as,

$$\frac{1}{T_1} = \frac{16\pi\mu^3 M_s \left(k_B T_{\text{sp}}\right) k_1 F\left(\theta\right) 3D}{3Dh^2\omega_0} \tag{11}$$

where $M_s \approx 200$ for YIG, the spin wave stiffness is $D = 0.55 \times 10^{-28}$ erg, the minimum wave vector $k_1 \approx 2\pi/d$ (where d is the grain $\approx$ domain size), ω_0 the resonance frequency and $F(\theta)$ an angular factor characteristic for a spherical sample. Their estimates, if spin and lattice systems are in equilibrium, resulted in $(1/T_1) = 0.74 \times 10^5 T_{sp}$ which agreed with observed value.

8.2.2 Spin dynamics and anisotropic 2-magnon creation in $FeSi_3$

For the optimization of modern magnetic nano-scale devices, used for spintronics, etc., it is important to understand linear and nonlinear processes that contribute to magnetic relaxation. Zakeri et al. [94] studied epitaxial Fe_3Si films by ferromagnetic resonance and identified two relaxation channels, (1) dissipative isotropic Gilbert damping and (2) anisotropic two-magnon scattering, which could be separated by variation of the FMR frequency and the applied field direction. The results were expressed in terms of different contributions to the FMR linewidth:

$$\Delta B = \Delta B_{\text{Gilbert}} + \Delta B_{\text{Mosaic}} + \Delta B_{\text{2mag}} + \Delta B_{\text{inhom}} \tag{12}$$

The Gilbert damping appears, with strength λ, in the equation describing the motion of the magnetization $\mathbf{M}$: $d\mathbf{M}/dt = -\gamma\ \mathbf{M} \times \mathbf{B}_{\text{eff}} - \lambda\mathbf{M} \times (\mathbf{M} \times \mathbf{B}_{\text{eff}})$, where $\mathbf{B}_{\text{eff}}$ is an effective field consisting of the externally applied field and internal fields. The Gilbert term is linear in frequency ω, the mosaic term disappears for fields along the easy and hard axes of magnetization, the two-magnon contribution arises when a $\mathbf{k} = 0$ magnon excited by the FMR scatters into degenerate states of magnons having wave-vectors $\mathbf{k} \neq 0$ and the last term, which is caused by sample imperfections, was found to be small and largely independent of the varied parameters.

The experiments were conducted at room temperature. Selected data from Zakeri et al.'s experiments on $FeSi_3$ grown by molecular beam epitaxy on MgO [001] are shown in Fig. 31. Table 2 shows the different contributions

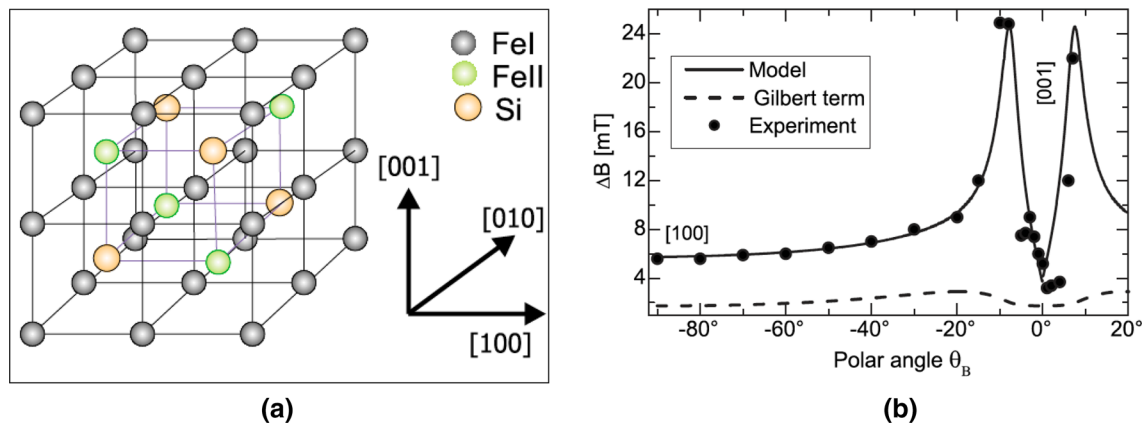**Fig. 31 a** Crystal structure of $FeSi_3$, **b** the variation of linewidth with the polar angle between applied field and the [001] axis. Corresponding data were recorded for the [110] axis and led to the conclusion that the damping due to two-magnon scattering was dominating. From [94]

Table 2 Contributions to FMR linewidth (extracted from [94])

Sample	Gilbert damping $\Delta B_{\mathrm{Gilbert}}$ [10^7 Hz]	Two-phonon along $< 100 >$ $\Delta B_{2\mathrm{mag}}$ [10^7 Hz]	Two-phonon along $< 110 >$ $\Delta B_{2\mathrm{mag}}$ [10^7 Hz]
40 nm Fe$_3$Si, as prepared	5.1	53 (17)	26 (2)
8 mm Fe$_3$Si, annealed	5.1 (1)	25 (2)	4 (2)
8 mm Fe$_{0.80}$Si$_{0.20}$, annealed	5.8	7 (2)	2.65 (5)

to linewidth, with the $< 100 >$ two-magnon dominating. This scattering (which occurs on imperfections in the lattice) could be reduced by annealing. The linewidths are about 10^8 Hz at room temperature, which corresponds to spin relaxation times of the order of 10 ns.

9 Summary and outlook

Spin spectroscopy has served science and society during 75 years with much detailed information, often not obtainable by other means. An essential part of this information concerns internal dynamics of molecular systems, particle motion in liquids and solids, spin ordering and collective excitations in magnetic systems, obtained by recording spin relaxation with increasingly refined techniques. Information covers a dynamical time range from seconds down to femtoseconds.

The present review traces the origin of several of these techniques and gives examples of its progress in different fields of application. Although coming of age, spin spectroscopy is still showing its usefulness as a complement to modern spectroscopies based on synchrotron radiation and other accelerator-based techniques, where the studied systems are regarded from other perspectives. Recent applications include studies and control of qubits in quantum computing elements and information of relevance for spintronics.

References

1. J. W. Emsley and F. James, Milestones in the first fifty years of NMR, in *Progress in Nuclear Magnetic Resonance Spectroscopy* **28**, 1 (1995)
2. D. ter Haar, *The Old Quantum Theory*, Pergamon Press. p. 206 (1967)
3. T. Preston, *The Scientific Transactions of the Royal Dublin Society*, 2nd series. **6**, 385 (1898)
4. A. Landé, Z. Phys. **7**, 398 (1921)
5. G. E. Uhlenbeck, S. Goudsmit, Naturwissenschaften **47** 953 (1925)
6. G. E. Uhlenbeck, S. Goudsmit, Nature **117**, 264 (1926)
7. W. Pauli, Z. Physik **31**, 373 (1925)
8. W. Pauli, Z. Physik. **31**, 765–783 (1925)
9. P. A. M. Dirac, Proc. R. Soc. Lond. Ser. A, **117 (778)**, 610 (1928)
10. W. Gerlach, O. Stern, Z. Physik **9**, *349* (1922)
11. T. E. Phipps, J. B. Taylor, Phys. Rev. **29** (2), 309 (1927)
12. R. Frisch, E. Segré, Z. Phys. **80**, 610 (1933)
13. I. I. Rabi, Phys. Rev. **49**, 324 (1935)
14. R. S. Shankland, Phys. Today **27**, 37 (1974)
15. H. Kopfermann, Z. Phys. **83**, 417 (1933)
16. E. Fermi, Z. Phys. **60**, 320 (1930)
17. W. E. Blumberg, J. Eisinger, M. P. Klein, Phys. Rev. **124**, 206 (1961)
18. I. I. Rabi, J. R. Zacharias, S. Millman, P. Kusch, Phys. Rev. **55**, 5267 (1939)
19. J. M. Kellogg, I. I. Rabi, N. F. Ramsey, J. R. Zacharias, Phys. Rev. 56, 728 (1939)
20. E. M. Purcell, H. C. Torrey, R. V. Pound, Phys. Rev. **69**, 37 (1946)
21. F. Bloch, W. W. Hansen, M. Packard, Phys. Rev. **69**, 127 (1946)
22. J. Larmor, *British Physicist*, pp. 1847–1942, http://www.universityscience.ie/pages/scientists/sci_josephlarmor.php
23. E. L. Hahn, Phys. Rev. **80**, 580 (1950)
24. R. R. Ernst and W. A. Andersson, Rev. Sci. Instrum. **37**, 93 (1966)
25. R. R. Ernst, in *The Application of Computer Techniques in Chemical Research*, The Institute of Petroleum, London 1972, p. 61
26. J. Jeener, P. Broekart, Phys. Rev. **157**, 232 (1967)
27. J. Jeener, B. H. Meier, P. Bachmann and R. R. Ernst, J. Chem. Phys.**71**, 4546 (1979)
28. K. Schmidt-Rohr, H. W. Spiess, Phys. Rev. Lett. **66,** 3020 (1991)
29. U. Tracht, M. Wilhelm, A. Heuer, H. Feng, K. Schmidt-Rohr, H.W. Spiess, Phys. Rev. Lett. **81**, 2727 (1998)
30. E. Matthias, B. Olsen, D. A. Shirley, T. E. Templeton, R. M. Steffen, Phys. Rev. **A4**, 1626 (1971)
31. M. Savukov, M. V. Romalis, Phys. Rev. Lett. **94**, 123001 (2005)
32. E. K. Zavoisky, *Paramagnetic Relaxation of Liquid Solutions for Perpendicular Fields. J. Exp. Theor. Phys.*, **15**, 344 (1945)
33. A. Abragam and B. Bleaney, *Electron Paramagnetic Resonance of Transition Ions*, Oxford University Press, 1970 (Reissue 2012)
34. *High Resolution EPR; Applications to Metalloenzymes and Metals in Medicine* (eds. R. Berliner, G. Hanson), Springer Nature Publ. (2020)
35. F. Bloch, Phys. Rev. **70**, 460 (1946)
36. E. M. Bloembergen, R. V. Purcell, Pound, Phys. Rev. **73**, 679 (1948)
37. A. Abragam, *Principles of Nuclear Magnetism* (Oxford University Press, 1961)
38. H. Y. Carr and E. M. Purcell, Phys. Rev. **94**, 630 (1954)
39. J. G. Powles, H. S. Gutowsky, J. Chem. Phys. **23**, 1692 (1955)
40. H. W. Spiess, *Dynamic NMR Spectroscopy* Ch. 2: "Rotation of Molecules and Nuclear Spin", Springer, Berlin-Heidelberg (1978)
41. R. Damadian, Science **171**, 1151 (1971)
42. E. Odeblad, U. Bryhn, Acta Radiologica **47**, 315 (1957)
43. P. C. Lauterbur, Nature **242**, 190 (1973). https://doi.org/10.1038/242190a0.
44. J. Mattson, M. Simon, *The Pioneers of NMR*, p. 65, Bar-Ilan University Press, Jericho NY, USA (1996)
45. A. N. Garraway, P. K. Grannell, P. Mansfield, J. Phys. C Solid State Phys. **C7**, L457 (1974)
46. R. R. Ernst, Rev. Sci. Instrum. **37**, 93 (1966). https://doi.org/10.1063/1.1719961
47. R. Messer, D. Höpfel, C. Schmidt, A. Seeger, W. Zag, Z. Phys. Chemie **145**, 4335 (1985)
48. C. P. Gray and N. Dupré, Chem. Rev. **104**, 4493 (2004)
49. "NSF: Abt Report on "The Emergence of Tissue Engineering as a Research Field". http://www.nsf.gov
50. S. F. Edwards and T. A. Vilgis, Rep. Prog. Phys. **51**, 243 (1988)
51. P. G. de Gennes, *Scaling Concepts in Polymer Physics*, Cornell UP, Ithaca, New York (1979)
52. N. F. Fatkullin, T. Körber, E. A. Rössler, Polymer **142**, 310 (2018)
53. K. Wüthrich, Nobel Lecture (2002), http://www.nobelprize.org/wutrich-lecture
54. T. R. Alderson and L. E. Kay, Cell **184**, 577 (2021)
55. D. Ban, T. M. Sabo, C. Griesinger and D. Lee, Molecules **18**, 11904 (2013)

56. J. P. Loria, M. Rance and A. G. Palmer III, J. Biomol. NMR **15**, 151 (1999)
57. K. Pervushin, R. Riek, G. Wider, and K. Wüthrich, PNAS **94** 1236671 (1997)
58. R. P. Feynman, Int J. Theor. Phys. **21**, 467 (1982). https://doi.org/10.1007/BF02650179
59. J. P. Dowling and G. J. Milburn, Phil. Trans. R. Soc. Lond. **361**, 1655 (2003)
60. R. M. Serra and I. S. Oliviera, Phil. Trans. R. Soc. A **370**, 4615–4619 (2012). https://doi.org/10.1098/rsta.2012.0332
61. L. M. Vandersypen, M. Steffen, G. Breyta, C. S. Yannoni, M. H. Sherwood, I. L. Chuang, Nature, **414**, 883 (2001)
62. L. M. Vandersypen, A. Wallraff, https://qudev.phys.ethz.ch/static/content/QSIT12/QSIT12_NMR_L01.pdf
63. C. E. Bradley, J. Randall, M. H. Abobeih, R. C. Berrevoets, M. J. Degen, M. A. Bakker, M. Markham, D. J. Twitchen, and T. H. Taminiaul, Phys. Rev. X **9**, 031045 (2019)
64. D. R. Hamilton, Phys. Rev. **58**, 122 (1940)
65. E. Matthias, D. A. Shirley, and R. A. Naumann, Phys. Rev. B. **140**, 264 (1965)
66. E. B. Karlsson, *Solid State Phenomena, As Seen by Muons, Protons and Excited Nuclei,* Oxford University Press (1995)
67. G. Goertzel, Phys. Rev. **70**, 897 (1946)
68. H. Aeppli, H. Albers-Schönberg, A. S. Bishop, H. Frauenfelder, E. Heer, Phys. Rev. **84**, 370 (1951)
69. P. B. Hemmig, R. M. Steffen, Phys. Rev. **92**, 832 (1953)
70. A. Abragam and R. V. Pound, Phys. Rev. **92**, 943 (1953)
71. R. M. Suter and C. Hohenemser, Phys. Rev. Lett. **41**, 705 (1978)
72. A. M. Gottlieb and C. Hohenemser, Phys. Rev. Lett. **31**, 1222 (1973)
73. A. Schenck, *Muon Spin Rotation Spectroscopy*, Adam Hilger Ltd., Bristol (1985)
74. A. Yaouanc and P. Dalmas de Réotier, *Muon Spin Rotation, Relaxation and Resonance*, Oxford Univ Press. Press (2016)
75. E. B. Karlsson, Eur. Phys. J. H **39**, 303 (2014)
76. E. Karlsson, O. Hartmann and B. Hjörvarsson, Hyperfine Interact. **105**, 211 (1997)
77. K. W. Kehr, D. Richter, J.-M. Welter, O. Hartmann, E. Karlsson, L. O. Norlin, Phys. B. 26, 567 (1982)
78. E. Karlsson, R. Wäppling, S. W. Lidström, O. Hartmann, R. Kadono, R. F. Kiefl, R. Hempelmann, D. Richter, Phys. Rev. B **52**, 6217 (1995)
79. O. Hartmann, E. Karlsson, R. Wäppling, J. Chappert, A. Yaouanc, L. Asch, G. M. Kalvius, J. Phys. F: **16**, 1593 (1986)
80. J. W. Cable, R. M. Nicklow and N. Wakabayashi, J. Magn. Magn. Mater. **54**, 1173 (1987)
81. E. Wäckelgård, O. Hartmann, E. Karlsson, R. Wäppling, L. Asch, G. M. Kalvius, J. Chappert, A. Yaouanc, UUIP (Uppsala University Department of Physics) Report -1160 (1987)
82. R. Wäppling, O. Hartmann, S. Harris, E. Karlsson, G. M. Kalvius, L. Asch, J. Magn. Magn. Mater. **119**, 123 (1993)
83. E. Lidström, R. Wäppling, O. Hartmann, M. Ekström, G. M. Kalvius, J. Phys.: Condens. Matter **8**, 6281 (1996)
84. G. Feher, Phys. Rev. **103**, 834 (1956)
85. A. Schweiger and G. Jeschke, *Principles of Pulse Electron Paramagnetic Resonance*, Oxford University Press (2001)
86. J. Messinger, J. H. Robblee, C. Fernandez, R. M. Cinco, H. Visser, U. Bergmann, P. Glatzel, S. P. Cramer, K. A. Campbell, J. M. Peloquin, R. D. Britt, K. Sauer, V. K. Yachandra, M. P. Klein, pp. 1279–1282 in *Photosynthesis: Mechanisms and Effects*, (editor G. Garab), Kluwer, Dordrecht (1998)
87. H. J. Halpern, C. Yu, M. Peric, E. Barth, D. J. Grdina, B. A. Teichler, PNAS 91, 13047 (1994)
88. S. S. Eaton, G. R. Eaton, J. Magn. Res. 223, 151 (2012)
89. K. C. Miao, J. P. Blanton, C. P. Anderson, A. Bourassa, A. L. Crook, G. Wolfowic, A. Hiroshi, T. Ohshima, D. D. Awschalom, Science **369**, 1493 (2020)
90. J. N. E. Griffiths, Nature **158**, 670 (1946)
91. C. Kittel, Phys. Rev. **73**, 155 (1948)
92. E. G. Spencer, R. C. Le Craw, Phys. Rev. Lett. 4, 130 (1960)
93. M. Sparks, C. Kittel, Phys. Rev. Lett. **4**, 232 (1960)
94. Kh. Zakeri, H. J. Halpern, C. Yu, M. Peric, E. Barth, D. J. Grdina, B. A. Teicher, J. Rocker, S. S. Kalarickal, K. Lenz, W. Kuch, K. Baberschke, Z. Frait, Phys. Rev. B **76**, 104416 (2007)